A numerical unit cell model for predicting the failure stress state of vertically perforated clay block masonry under arbitrary in-plane loads

Raphael Reismüller [a],*, Markus Lukacevic [a], Sebastian Pech [a], Andreas Jäger [b], Josef Füssl [a]

[a] *Institute for Mechanics of Materials and Structures, TU Wien, Karlsplatz 13/202, 1040, Vienna, Austria*
[b] *Wienerberger AG, Wienerbergerplatz 1, 1100, Vienna, Austria*

ARTICLE INFO

ABSTRACT

As vertically perforated clay block masonry advances into more demanding building categories, knowledge of the effective masonry strength under different loading states becomes crucial. However, experimentally identifying macroscopic failure surfaces for such masonry requires a massive effort. In this study, we propose a FEM-based simulation concept to predict failure stress states of masonry under arbitrary in-plane loading. The proposed concept is validated using seven experiments from the literature. Subsequently, subjecting the validated model to various load cases allows for deriving a failure surface comparable to the Rankine–Hill surface. Thus, by applying the presented concept, we can effectively generate macroscopic failure surfaces for any perforated clay block design.

1. Introduction

Being one of the oldest materials in human history, clay block masonry remains a popular material for its low thermal conductivity, durability, fire resistance, and ease of construction, particularly in residential and low-rise buildings. In recent years, the construction industry has increasingly focused on reducing its carbon footprint, which has highlighted the challenge of reducing CO_2 emissions in the fabrication process of fired clay blocks. Therefore, new ways to optimize the production process and the products themselves are being considered [1–4].

Moreover, although masonry offers numerous benefits, it has recently fallen behind other traditional materials, such as steel and concrete, when it comes to the accessibility and simplicity of structural analysis using finite element (FE) software. This is partly due to the challenge of acquiring effective strength parameters under different loading conditions for the great variety of modern masonry products. As an increasing number of structural engineers depend on the conveniences provided by modern FE software, it is crucial to develop new methods for obtaining these strength parameters to calibrate effective failure surfaces.

Although there are several approaches for defining failure surfaces for masonry, only a few of them apply to vertically perforated clay block masonry. One of these surfaces was proposed by Ganz [5], who analytically defined twelve failure criteria (see Appendix A). Thereby, he considered different failure mechanisms typically occurring in masonry structures and derived criteria from the geometry of the blocks

and the material properties. Another approach is the Rankine–Hill surface developed by Lourenço [6], which is one of the most widely used approaches for simulating the behavior of masonry structures under different loading conditions (refer to [7–14]). The Rankine–Hill surface consists of two parts: a Hill-type criterion for compressive failure and a Rankine-type criterion for shear and tensile failure (see Appendix B). Both criteria were developed to qualitatively model the experimentally observed failure behavior of a masonry wall without considering specific failure mechanisms.

To calibrate such failure surfaces, macroscopic experiments that characterize the material's behavior under different loading conditions are required. This is already a complex task for a few selected loading states. In addition, the product palette of masonry is becoming increasingly diverse, thus, making an experimental identification of the failure surfaces impossible. One solution to this challenge is the use of reliable numerical models to simulate the needed macroscopic experiments for the calibration of the surfaces. Such accurate simulations of the masonry's behavior under different loading conditions provide a more efficient and cost-effective alternative to conducting physical experiments.

Using computational methods for predicting the behavior of masonry is getting more and more attention [15–22]. Recently, Kiefer et al. [23] proposed an FE-based approach to predict the compressive strength of vertically perforated clay block masonry. Using the eXtended Finite Element Method (XFEM) [24] and the orthotropic

---

* Corresponding author.
E-mail address: raphael.reismueller@tuwien.ac.at (R. Reismüller).

Hoffman criterion [25] in combination with a unit cell approach and periodic boundary conditions, they were able to accurately predict the vertical compressive strength of eight different block designs. In this study, we enhance this numerical model by adding additional failure mechanisms to depict the failure under arbitrary in-plane loading scenarios.

For validation of the numerical model, a set of experiments is necessary. Recently, Bitterli and Salmanpour [26,27] published a suitable experimental study for vertically perforated clay block masonry, in which they did seven compressive tests on wall specimens with inclined bed joints. Although the specimens were loaded uniaxially, changing the incline angle from 0° to 90° in steps of 15° led to different combinations of compressive and shear stresses orthogonal to the joint system. In these experiments, they identified the key failure mechanisms under combined compressive and shear loads and a relation between the bed joint incline and the obtainable peak stress. Thus, we used these experiments for the validation of the presented numerical model.

The outline of the work is as follows: First, we enhanced the numerical model developed by Kiefer et al. [23] by introducing a failure criterion for the mortar joints. For this, we back-calculated the damage properties of the mortar joints by simulating shear tests on masonry triplets [26,27]. Secondly, we validated the model by simulating the experiments conducted by Bitterli and Salmanpour [26,27] using the FE software Abaqus. The numerically obtained failure stress states matched the experimental results and the key failure mechanisms could be replicated in our simulations. After proving the validity of the model, we simulated additional loading combinations on the same model to calibrate the failure surfaces following Ganz [5] and Lourenço [6]. The obtained failure surfaces showed good agreement with the simulations used for validation. Therefore, the model has the potential to substitute experiments for calibrating failure surfaces.

Section 2 contains an overview of the applied modeling strategies and the numerical model. The application of these modeling strategies for simulating the verification experiments is provided in Section 3. Afterward, the results are explained and discussed in Section 4, followed by conclusions in Section 5.

2. Modeling strategies

While *solid* clay block masonry was already used 5000 years ago, *vertically perforated* clay blocks are nowadays commonly used in Central Europe because of their improved properties and material efficiency. A pattern of vertical cavities is introduced to the solid clay block, which creates a network of slender, plate-like webs. These webs are mostly orthogonal and can be categorized by their orientation (see also Fig. 1):

- Longitudinal webs are oriented parallel to the wall surface ($x - z$-plane),
- Transversal webs are oriented perpendicular to the wall surface ($y - z$-plane).

In general, masonry is constructed by putting prefabricated blocks together in a regular pattern, joined by an adhesive material between these blocks, to ensure a sufficient tensile and shear strength of the resulting structure. Traditionally, mortar was used for this purpose. Nowadays, other materials like polyurethane glue simplify the production process. Horizontal joints are referred to as *bed joints*, vertical ones as *head joints*. In terms of strength, these joints are a structural weakness; however, they are necessary for the structure's ductility, required to withstand cyclic shear loads e.g., during earthquakes.

2.1. Utilizing the periodicity of masonry — unit cell concept

Since vertically perforated clay block masonry is commonly built up in a periodic pattern, the use of a unit cell approach with periodic boundary conditions is possible. Hence, a unit cell concept was implemented, which was proposed by Kiefer et al. [23] and applied with
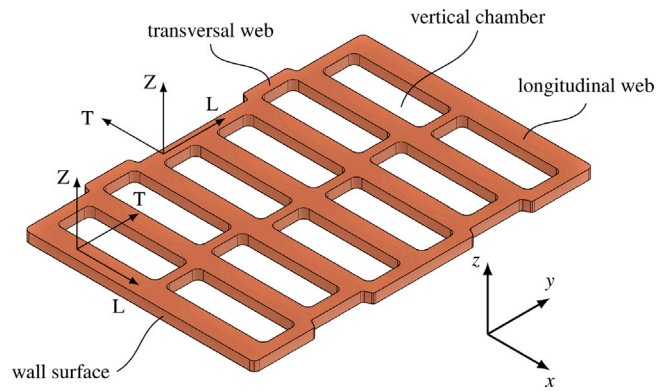

Fig. 1. Parts of a vertically perforated clay block and material orientation represented by the L-T-Z coordinate system (from [28]). While the Z-axis coincides with the *z*-axis, the L- and *T*-axis follow the orientation of the webs.

minor adaptions in [19]. Using this concept we can approximate the response of the entire specimen by modeling only a small part of the structure, the so-called *repeating unit cell*. Hence, the computation times can be kept short, although complex non-linear material models are used.

2.1.1. Defining a repeating unit cell

For simplifying the definition of the periodic boundary conditions within the FEM framework, a cuboid unit cell was chosen. The smallest cuboid unit cell found in a masonry wall with an offset of half a block's width is two blocks high and one block wide (see Fig. 2).

The following convention was used for referring to the surfaces, edges, and vertices of the unit cell [29]:

- Surfaces are denoted *North*, *South*, *East*, *West*, *Top*, and *Bottom*.
- The names of the edges and vertices consist of the first letters of the intersecting surfaces (e. g. *NW* and *SWB*).

The unit cell consists of six parts, which are segments of two full clay blocks. The dimensions of each part P1 to P6 are shown in Fig. 2(b). For modeling the mortar joints we decided to use a simplified micro-modeling approach [6]. Therefore, we modeled the blocks in full detail, while reducing the mortar joints to 2D interfaces between those blocks. When reducing the mortar joints to interfaces, the total dimensions of the unit cell can be kept constant by evenly distributing the thickness of each joint to the dimensions of the adjacent blocks [6]. Since increasing the web thickness would have a significant effect on the structural behavior, the thickness of the head joint was evenly distributed to the length of each cavity. The interaction properties for considering the mortar joints (see Section 2.2.2) were imposed on each surface in contact with another surface.

2.1.2. Periodic boundary conditions and homogenization

The repeating unit cell is two-dimensionally periodic, i. e., in *x*- and *z*-direction, using the same coordinate system as shown in Fig. 1. The vectors $\mathbf{c}_x$ and $\mathbf{c}_z$ describe this periodicity and contain essentially the dimension of the unit cell in the given direction. To ensure geometric compatibility between the neighboring instances of the unit cell in the deformed state, periodic boundary conditions were applied on the periodic surfaces. These periodic boundary conditions are linear equations, which couple the displacements of each pair of corresponding points on opposing surfaces to the displacements of the primary nodes of the unit cell. Hence, the displacement of a point *A* on surface *South* is coupled to the displacement of the opposing point *B* on surface *North* and the displacements of the primary nodes. The same applies to each point on surface *East* and the opposing point on surface *West*. In contrast, the surfaces *Top* and *Bottom* may deform freely. A more
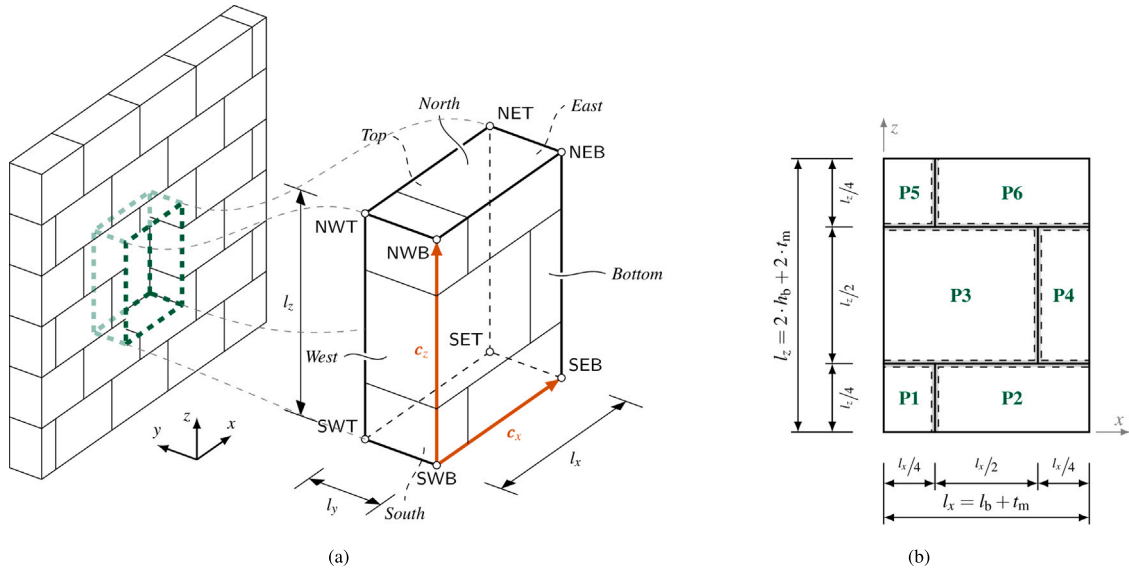
Fig. 2. Composition and geometry of the chosen repeating unit cell as part of the entire structure (a) and dimensions of the six fired clay parts (b). The naming convention in (a) is based on the suggestions from Böhm [29].

Table 1
Primary node displacements for imposing effective strain states.

	Strain state	Primary node displacement
LC1	$\begin{bmatrix} \epsilon_{xx} & 0 \\ 0 & 0 \end{bmatrix}$	*Horizontal uniaxial strain* $u_x^{SEB} = \bar{\epsilon}_{xx} \cdot l_x, \quad u_x^{SET} = \bar{\epsilon}_{xx} \cdot l_x$
LC2	$\begin{bmatrix} 0 & 0 \\ 0 & \bar{\epsilon}_{zz} \end{bmatrix}$	*Vertical uniaxial strain* $u_z^{NWB} = \bar{\epsilon}_{zz} \cdot l_z, \quad u_z^{NWT} = \bar{\epsilon}_{zz} \cdot l_z$
LC3	$\begin{bmatrix} 0 & \bar{\epsilon}_{xz} \\ \bar{\epsilon}_{xz} & 0 \end{bmatrix}$	*Pure shear strain* $u_z^{SEB} = \bar{\epsilon}_{xz} \cdot l_x, \quad u_z^{SET} = \bar{\epsilon}_{xz} \cdot l_x$ $u_x^{NWB} = \bar{\epsilon}_{xz} \cdot l_z, \quad u_x^{NWT} = \bar{\epsilon}_{xz} \cdot l_z$

The following primary node displacements were imposed in each case:
$u_x^{SWB} = u_y^{SWB} = u_z^{SWB} = 0, \; u_x^{SWT} = u_z^{SWT} = 0, \; u_y^{SEB} = 0, \quad u_y^{NWB} = 0.$

detailed explanation of the implementation of the periodic boundary conditions is given in Suda et al. [19].

Using periodic boundary conditions, the deformation difference **Δu** between two surfaces is constant [30]. Hence, for prescribing a deformation-controlled loading on the repeating unit cell, this deformation difference has to be defined for only two pairs of nodes per periodicity direction: the primary nodes (e. g., *SWB-NWB* and *SWT-NWT* in z-direction). By systematically controlling these deformation differences, we can impose effective in-plane strain states on the unit cell (see Table 1). Thus, we can simulate arbitrary macroscopic in-plane strain states $\bar{\epsilon}$ by combining the load cases in Table 1. These macroscopic strains applied to the FE model enable the identification of microscopic strains ϵ on the detailed geometry. The microscopic strains lead to microscopic stresses σ in the FE model, which we homogenize to macroscopic stresses $\bar{\sigma}$.

The deformation difference Δu_i is related to the macroscopic strain state $\bar{\epsilon}$ through the periodicity vector c_i:

$$\Delta u_x = \bar{\epsilon} \cdot c_x = \begin{pmatrix} \bar{\epsilon}_{xx} \cdot l_x \\ \bar{\epsilon}_{xy} \cdot l_x \\ \bar{\epsilon}_{xz} \cdot l_x \end{pmatrix} \quad \text{and} \quad \Delta u_z = \bar{\epsilon} \cdot c_z = \begin{pmatrix} \bar{\epsilon}_{xz} \cdot l_z \\ \bar{\epsilon}_{yz} \cdot l_z \\ \bar{\epsilon}_{zz} \cdot l_z \end{pmatrix}, \quad (1)$$

with the dimensions of the repeating unit cell in x- and z-direction, l_x and l_z, respectively. Prescribing zero displacements at primary nodes *SWB* and *SWT* allows us to fully prescribe the calculated deformation difference at the opposing node, which leads to the relations in Table 1.

2.1.3. Stress homogenization

The macroscopic stress state is the main result we wanted to obtain from the simulations. In each point on the surface of the unit cell,

multiplying the macroscopic stress tensor $\bar{\sigma}$ with the surface normal vector $n(x)$ leads to the traction stress vector $t(x)$. Since the macroscopic stresses are considered constant over the repeating unit cell, these traction stresses are also constant for points with the same surface normal vector. Integrating the macroscopic traction stresses t over one surface S_i of the repeating unit cell leads to the total amount of forces acting on this surface:

$$F^i = \int_{S_i} \bar{\sigma} \cdot n_i \, dS = \bar{\sigma} \cdot n_i \cdot A_i. \quad (2)$$

Since the displacements are only prescribed at the primary nodes, the traction forces for a surface are essentially the sum of reaction forces occurring at the primary nodes located on this surface. Evaluating Eq. (2) for surfaces *East* with n pointing in positive x-direction, and *North* with n pointing in positive z-direction leads to the following relations:

$$F^E = F^{SEB} + F^{SET} = \begin{pmatrix} \bar{\sigma}_{xx} \\ \bar{\sigma}_{xy} \\ \bar{\sigma}_{xz} \end{pmatrix} \cdot A_E \quad \text{and} \quad (3)$$

$$F^N = F^{NWB} + F^{NWT} = \begin{pmatrix} \bar{\sigma}_{xz} \\ \bar{\sigma}_{yz} \\ \bar{\sigma}_{zz} \end{pmatrix} \cdot A_N. \quad (4)$$

Hence, the macroscopic stress tensor can be obtained from the reaction forces at the primary nodes as

$$\bar{\sigma} = \begin{bmatrix} \dfrac{F_x^{SEB} + F_x^{SET}}{A_E} & \dfrac{F_z^{SEB} + F_z^{SET}}{A_E} \\ \dfrac{F_x^{NWB} + F_x^{NWT}}{A_N} & \dfrac{F_z^{NWB} + F_z^{NWT}}{A_N} \end{bmatrix}. \quad (5)$$

It is important to note that the unit cell concept and the homogenization procedure require a homogeneous stress state across the unit cell's dimensions. Consequently, the applicability of these methods is primarily limited to larger masonry walls where this condition can be met. Conversely, when dealing with smaller structures, it is advisable to consider a more detailed micro-modeling approach.

2.2. Failure mechanisms implemented in the finite element model

Both clay block failure and joint failure are relevant for the structural collapse of vertically perforated clay block masonry under in-plane loading. The clay blocks mostly fail due to tensile cracks in the transversal or longitudinal webs [19,23,31]. For the mortar joints,

shear failure or tensile failure (or a combination of both) can be relevant, depending on the stress component perpendicular to the joint [32]. Based on these observations, the following failure mechanisms were implemented in the numerical model.

2.2.1. Brittle failure of fired clay

For the brittle failure of the fired-clay blocks a combination of the XFEM [24], the orthotropic Hoffman criterion [25], and the Virtual Crack Closure Technique (VCCT) [33,34] was used. This strategy was proposed by Kiefer et al. [23] and was successfully applied in another study [19]. The XFEM approach uses special displacement functions at so-called *enriched nodes*, which allow the modeling of discrete propagating cracks without re-meshing. For initiating such cracks, the orthotropic Hoffman criterion is used, which takes into account the material's tensile, compressive, and shear strengths (see C). Using this formulation, the failure criterion cannot capture triaxial compressive failure. Since the webs can be considered plate-like structures, which are not loaded perpendicular to their surface, the stress state in the webs is nearly plane. Therefore, triaxial compressive failure is not relevant in this case. After a crack is initiated, a *crack evolution criterion*, in our case the VCCT, depicts the onset of the crack. Details on the implementation of XFEM and VCCT in Abaqus can be found in the Abaqus Online Documentation [35].

Considering orthotropic material behavior is essential for vertically perforated clay blocks, due to the orthotropic nature of extruded fired clay [4,36,37]. This orthotropy originates in the manufacturing process, where the raw material is extruded and cut into blocks. During the extrusion process, the flat clay minerals align parallel to the surface of the given part [36], leading to a locally changing coordinate system (L-T-Z) on the material level (see Fig. 1). Hence, the stiffness in T-direction is approximately 37 % to 60 % of the stiffness in Z-direction (see Buchner et al. [1]). Since the stiffness in L-direction is only insignificantly below the stiffness in Z-direction, considering the material as transversally isotropic is a reasonable approximation, as Buchner et al. [1] showed. Thus, the material's stiffness and strength were considered transversally isotropic in this work (see Tables 3 and 4).

The application of the VCCT is based on linear elastic fracture mechanics, which allows a good approximation of the brittle failure of fired clay. The main assumption of the VCCT is. that the strain energy released when opening a crack is equal to the strain energy needed to close the same crack [38]. Based on this assumption, the energy release rate G is calculated and compared to a critical value G_c. In the numerical model, a power law was used to consider all three failure modes:

$$f = \frac{G}{G_c} = \left(\frac{G_{\mathrm{I}}}{G_{\mathrm{I,c}}}\right)^a + \left(\frac{G_{\mathrm{II}}}{G_{\mathrm{II,c}}}\right)^b + \left(\frac{G_{\mathrm{III}}}{G_{\mathrm{III,c}}}\right)^c = 1. \tag{6}$$

Considering the findings of Bocca et al. [39], Hannawald [40], as well as Eis and Vassilev [41], lower and upper limits for the mode-I fracture energy are $G_{\mathrm{I,c}}^{\min} = 0.01\,\mathrm{J/mm^2}$ and $G_{\mathrm{I,c}}^{\max} = 0.05\,\mathrm{J/mm^2}$. Since mode-I failure is governing, the fracture energies for modes II and III were chosen 20 times larger, following Kiefer et al. [23]. The superscripts a, b, and c were all set to 1.

2.2.2. Failure of the mortar joints

The shear behavior of mortar joints was thoroughly analyzed by Van der Pluijm [42]. He not only published comprehensive testing data on the strengths but also on the post-peak behavior including fracture energy values. According to Van der Pluijm [42] the shear strength $\tau_{\mathrm{m,f}}$ of a mortar joint follows a Mohr–Coulomb law:

$$\tau_{\mathrm{m,f}} = \tau_{\mathrm{m,ini}} - \mu_{\mathrm{m}} \cdot \sigma_{\perp}, \tag{7}$$

with the initial shear strength $\tau_{\mathrm{m,ini}}$, the frictional parameter μ_{m}, and the stress component perpendicular to the joint, $\sigma_{\perp}$. Hence, the shear strength increases with increasing compressive stresses perpendicular

to the joint and decreases vice versa. With increasing tensile stresses the shear strength eventually reaches zero.

In displacement-controlled shear tests Van der Pluijm [42] observed a damage evolution, which can be sufficiently described by an exponential relation. Furthermore, the remaining shear strength decreases until it reaches a constant residual strength value depending on the stress perpendicular to the joint.

We modeled the joints as interfaces using a surface-to-surface contact formulation [43,44]. For recreating the joint behavior we deployed a *cohesive behavior* approach in combination with frictional properties, a quadratic stress interaction damage criterion, and exponential damage evolution. A similar approach has been previously used by Bolhassani et al. [43] as well as Thamboo and Dhanasekar [44] for concrete block masonry. In line with Bolhassani et al., we combined the failure mechanisms of both the mortar and the interface into a single interface criterion. Consequently, the calibrated interface damage properties reproduce the decisive failure mechanism. Conversely, Thamboo and Dhanasekar modeled the mortar joints as three-dimensional continua, employing Concrete Damaged Plasticity for modeling mortar failure and the cohesive approach solely for considering interface failure. We opted for the simplified micro-modeling approach for several reasons. Notably, modeling a typical thin-layer mortar joint with a 1 mm thickness would necessitate an exceedingly fine mesh to maintain viable element aspect ratios. Additionally, this approach also allows for modeling modern joints bonded with polyurethane adhesives with minor adaptions.

The stiffness of the mortar joint is defined through the parameters K_{nn}, K_{ss}, and K_{tt}. These stiffness parameters control the relationship between the traction stresses t_i and the separations δ_i between the surfaces as

$$t_i = K_{ii}\delta_i, \quad \forall i \in \{n, s, t\}. \tag{8}$$

Thereby, n, s, and t define an orthogonal coordinate system with n pointing perpendicular to the joint. Thus, the $s-t$ plane is parallel to the joint. Considering isotropic material behavior, the stiffness parameters were derived from the Young's modulus E_{m} and the shear modulus G_{m} by multiplication with the joint thickness t_{m}:

$$K_{nn} = E_{\mathrm{m}} \cdot t_{\mathrm{m}}, \quad \text{and} \quad K_{ss} = K_{tt} = G_{\mathrm{m}} \cdot t_{\mathrm{m}} = \frac{E_{\mathrm{m}}}{2 \cdot (1 + \nu_{\mathrm{m}})} \cdot t_{\mathrm{m}}. \tag{9}$$

Notably, Eq. (8) only holds for positive contact clearance (see also the definition in the Abaqus Documentation [35]). For negative clearance (i. e. mortar deformations under compressive stresses) a tabular pressure-overclosure formulation was defined (see Fig. 3). Until reaching the compressive strength, tabular definition delivers the same pressure values as with the stiffness parameter K_{nn}. At the compressive strength of the mortar, a plateau is modeled. Since compressive mortar failure was only relevant in some small regions of the model for a limited number of cases, this simplified approach was sufficient to consider non-linear mortar behavior under compressive loads. An insignificant contact pressure at zero overclosure was implemented to overcome numerical problems when initiating contact.

Within the framework of cohesive behavior, the following quadratic stress interaction was used as a damage criterion:

$$\left(\frac{\langle t_n \rangle}{t_{\mathrm{f},n}}\right)^2 + \left(\frac{t_s}{t_{\mathrm{f},s}}\right)^2 + \left(\frac{t_t}{t_{\mathrm{f},t}}\right)^2 = 1, \tag{10}$$

with the traction stresses t_i and the traction strengths $t_{\mathrm{f},i}$. In compression, only the interaction of the shear stresses is considered since $\langle t_n \rangle$ is zero for negative tractions t_n. For implementing a similar relation as depicted by Van der Pluijm [42], we used an additional frictional parameter. With this frictional parameter the shear strengths in Eq. (10) are calculated using a Mohr–Coulomb relation and the contact pressure, leading to the following equation:

$$\left(\frac{\langle t_n \rangle}{t_{\mathrm{f},o}}\right)^2 + \left(\frac{t_s}{t_{\mathrm{f},o} - \mu_{\mathrm{m}} \cdot t_n}\right)^2 + \left(\frac{t_t}{t_{\mathrm{f},t} - \mu_{\mathrm{m}} \cdot t_n}\right)^2 = 1, \tag{11}$$
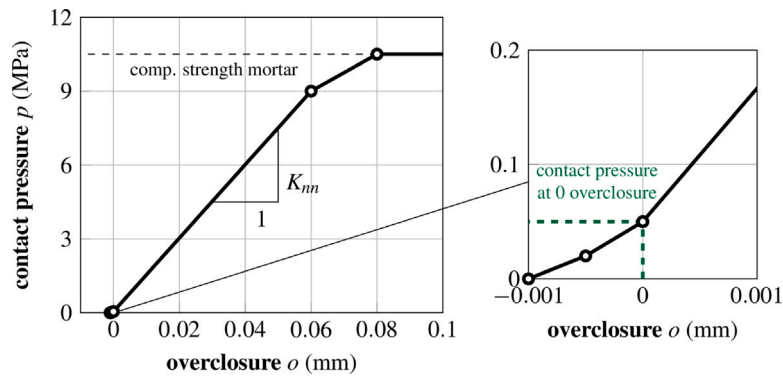
Fig. 3. Tabular pressure-overclosure formulation used for modeling the mortar joints in the simulations. A small artificial contact pressure at zero overclosure was implemented to overcome numerical problems when initiating contact.

which is simplified to

$$\left(\frac{\langle\sigma_\perp\rangle}{\sigma_{f,\perp}}\right)^2 + \frac{\tau^2}{\left(\tau_{m,ini} - \mu_m \cdot \sigma_\perp\right)^2} = 1, \quad (12)$$

with equal shear strengths $t_s^0 = t_t^0 = \tau_{ini}$ and the total shear stress $\tau^2 = t_s^2 + t_t^2$. Additionally, the traction in n-direction, t_n, and the corresponding strength $t_{f,n}$ were replaced by the stress component perpendicular to the joint, $\sigma_\perp$, and the tensile strength $\sigma_{f,\perp}$. The material parameters used in the simulations, i. e. peak strengths $\tau_{m,ini}$ and $\sigma_{f,\perp}$ as well as the friction coefficient μ_m, were back-calculated from shear tests and can be found in Section 3.

The exponential post-peak behavior observed by Van der Pluijm [42] was modeled by using a displacement-type exponential damage evolution within the cohesive-behavior property (see [35]). Here, two input parameters are necessary: the maximum displacement δ_m^{max} at which the strength reaches its minimum and an exponential parameter α. The maximum displacement was chosen with $\delta_m^{max} = 0.15\,mm$ leading to a fracture energy of $0.088\,J/mm^2$, matching the findings by Van der Pluijm [42]. The exponential parameter was set to $\alpha = 5$.

2.3. Failure criterion

For identifying peak stresses for an arbitrary macroscopic strain state a two-condition failure criterion was used. At the macroscopic scale, the stress state before the first significant decrease of a stress component was considered as macroscopic peak stress state $\bar{\sigma}^f$. This criterion was relevant, especially for joint failure, which occurs much more ductile than block failure. Furthermore, a second criterion considering the first crack within the blocks was defined to capture block failure. This was necessary, since some of the simulations, where block failure was relevant, did not produce a significant drop in stresses. Instead, these simulations aborted when the first crack opened. Considering the findings of Kiefer et al. [23] and Suda et al. [19], this is a good approximation, since there, the first crack also occurred just before the peak stress was reached.

3. Experiments and simulations

3.1. Experiments used for validation

For validating the numerical model we used an experimental study conducted by Bitterli and Salmanpour [26,27] (see Fig. 4). In the study, they did uniaxial compression tests on seven masonry specimens with inclined bed joints to investigate the behavior of vertically perforated block masonry under combined compressive and shear loads. The specimens were $1.20\,m$ high and $1.20\,m$ long (see Fig. 5(a)); the bed joint incline was varied from 0° (vertical compression) to 90° (horizontal compression) in increments of 15°. Within this study Bitterli

and Salmanpour obtained material strength and stiffness parameters depending on the bed joint incline and also described the changes in failure mechanisms. Each experiment is referred to by the angle of incline and a preceding "E", i. e., "E75" refers to the experiment with 75° incline.

Additionally, Bitterli and Salmanpour [26,27] conducted three shear tests on masonry triplets according to EN 1052-3 [46]. These tests were performed with three different levels of pre-compression. Hence, assuming the joint behavior follows a Mohr–Coulomb law, the initial shear strength $\tau_{m,ini}$ and the friction parameter μ_m could be obtained from the results.

Typical vertically perforated clay blocks (*Swissmodul B15/19*) from a Swiss manufacturer were used for the experiments (see Fig. 5(b)). These blocks were $290\,mm$ long, $190\,mm$ high, and $150\,mm$ wide, with a void ratio of 42%. In compressive tests according to EN 772-1 [47], they obtained a compressive block strength of $f_b = 26.3\,MPa$. The mortar used ("Weber mur 920 M15") is a ready-mixed general-purpose cement mortar. In flexural and compressive tests according to EN 1015-11 [48], Salmanpour [27] obtained a compressive strength of $f_m = 10.5\,MPa$ and a flexural strength of $f_{mq} = 2.8\,MPa$.

Each specimen was loaded cyclically with displacement-controlled loading phases and force-controlled unloading phases until the peak stress was reached. The loads were introduced by hydraulic jacks and distributed by two large spreader beams at the top and bottom of the specimen. Gypsum layers were placed between the spreader beams and the specimen to compensate for surface irregularities. On one surface of the specimen, digital image correlation (DIC) was used for obtaining strain information. On the opposite surface, the deformations were captured by five linear variable differential transformers (LVDTs). The forces used to calculate the resulting stresses were obtained from the testing machine.

The peak stresses obtained by Bitterli and Salmanpour [26,27] are plotted against the bed joint incline in Fig. 6. The vertical compressive strength f_{mz} (E00) was $5.35\,MPa$. With increasing incline, the compressive strength decreased drastically to 25% of f_{mz} at E45, whereafter it stayed nearly constant until E75. For E90 the compressive strength increased again to 38% of the vertical compressive strength. Hence, the largest peak stresses were obtained with predominant compressive loading perpendicular to the bed joint, while the smallest values were observed when the shear stresses reach their maximum.

Besides the peak stresses Bitterli and Salmanpour [26,27] also analyzed the crack patterns, failure mechanisms and stress–strain-relations. According to their observations, the behavior changed significantly with the bed joint incline. Specimens E00 and E15 failed very brittle, due to cracks in the transversal webs, leading to spalling of the outermost longitudinal webs. The stress–strain relation in z-direction was linear almost until collapse (see Fig. 14). Specimen E30 showed both cracks in the blocks and the joints and the failure was more ductile. In experiments E45, E60, and E75, joint failure was triggering
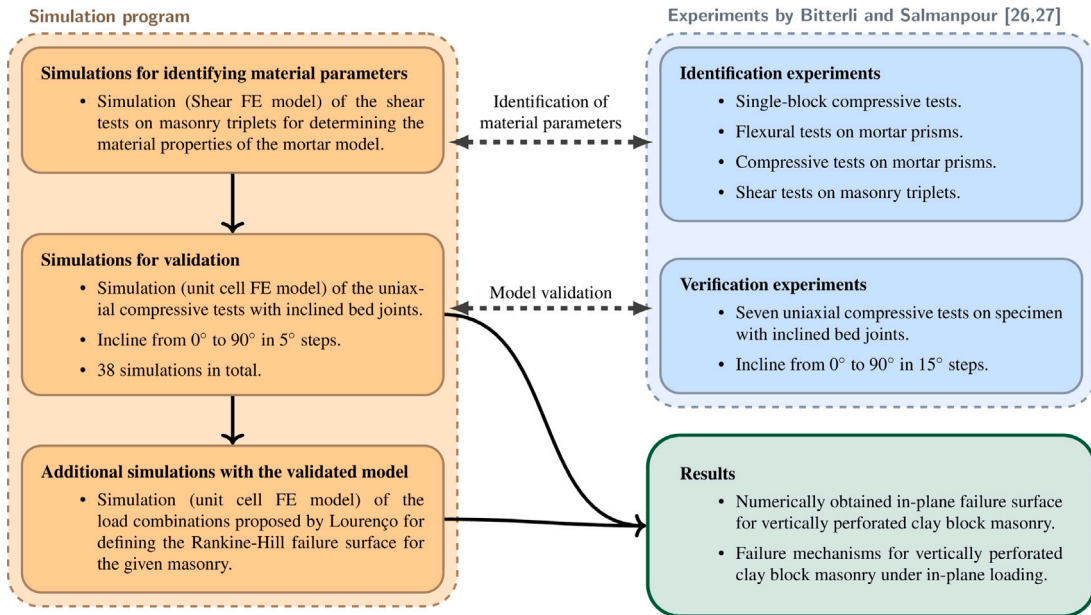
Simulation program

| **Simulations for identifying material parameters** |
| • Simulation (Shear FE model) of the shear tests on masonry triplets for determining the material properties of the mortar model. |

Experiments by Bitterli and Salmanpour [26,27]

| **Identification experiments** |
| • Single-block compressive tests. |
| • Flexural tests on mortar prisms. |
| • Compressive tests on mortar prisms. |
| • Shear tests on masonry triplets. |

Identification of material parameters

| **Simulations for validation** |
| • Simulation (unit cell FE model) of the uniaxial compressive tests with inclined bed joints. |
| • Incline from 0° to 90° in 5° steps. |
| • 38 simulations in total. |

Model validation

| **Verification experiments** |
| • Seven uniaxial compressive tests on specimen with inclined bed joints. |
| • Incline from 0° to 90° in 15° steps. |

| **Additional simulations with the validated model** |
| • Simulation (unit cell FE model) of the load combinations proposed by Lourenço for defining the Rankine-Hill failure surface for the given masonry. |

| **Results** |
| • Numerically obtained in-plane failure surface for vertically perforated clay block masonry. |
| • Failure mechanisms for vertically perforated clay block masonry under in-plane loading. |

Fig. 4. Overview of the modeling procedure.

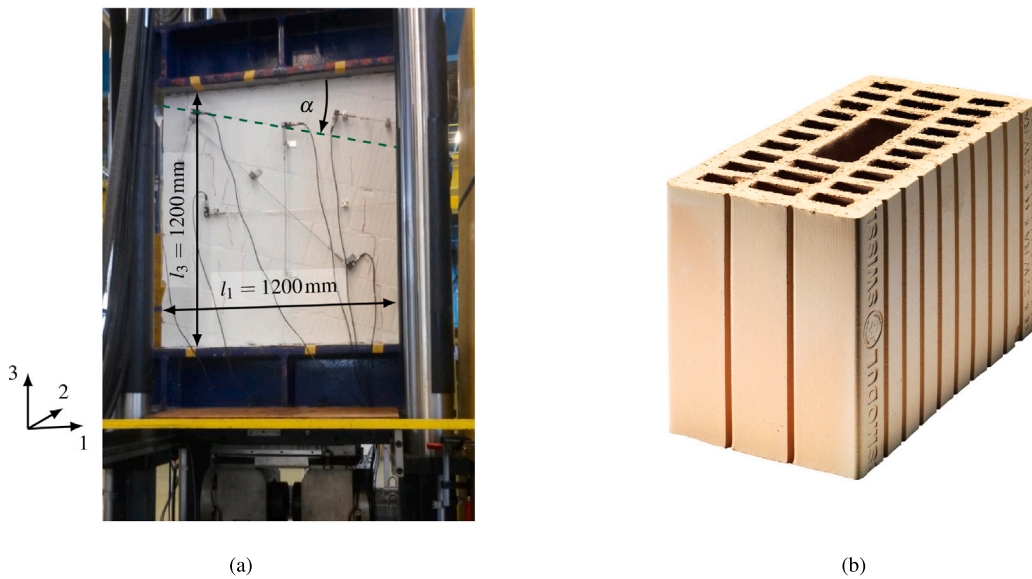(a)   (b)

Fig. 5. Experiments conducted by Bitterli and Salmanpour [26,27]: (a) experimental setup for E15 and (b) used clay block *Swissmodul B15/19*. *Source:* (Image from [45]).
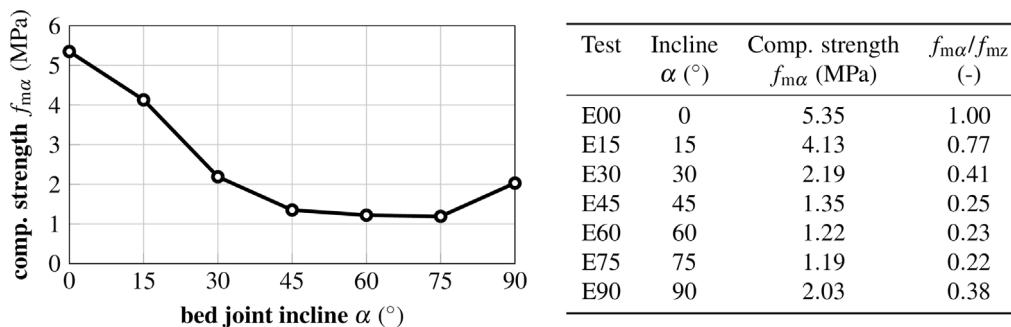

Test	Incline α (°)	Comp. strength $f_{m\alpha}$ (MPa)	$f_{m\alpha}/f_{mz}$ (-)
E00	0	5.35	1.00
E15	15	4.13	0.77
E30	30	2.19	0.41
E45	45	1.35	0.25
E60	60	1.22	0.23
E75	75	1.19	0.22
E90	90	2.03	0.38

Fig. 6. Experimentally obtained peak stresses with varying bed joint incline taken from Bitterli and Salmanpour [26,27].

- 6 fired-clay parts
- joints modeled as interface using surface-to-surface contact
- 146 646 nodes
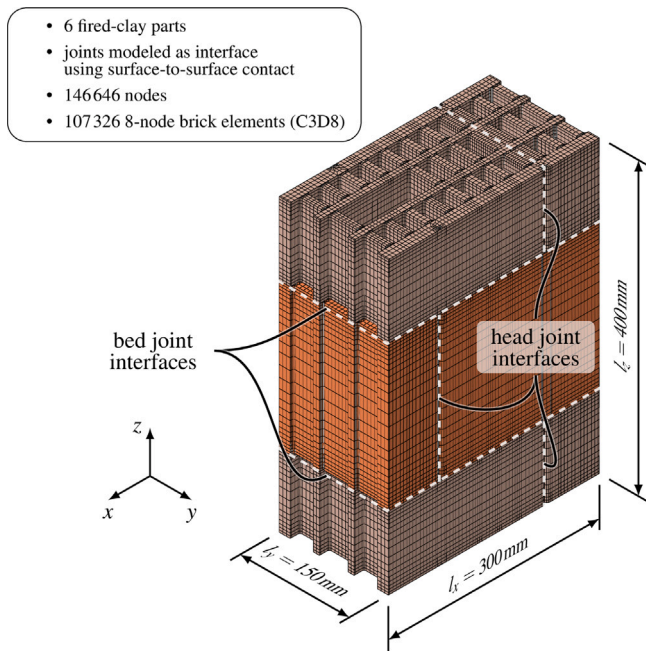- 107 326 8-node brick elements (C3D8)

Fig. 7. Unit cell finite element model used for the validation simulations (see also Fig. 4). The middle layer is colored differently to emphasize the different block layers with mortar interfaces in between.

collapse, as gliding planes in the bed joints started to form. The failure occurred even more ductile than for E30 and after the peak stress was reached, large strain values could be observed before collapse (see Fig. 14). Specimen E90 again failed brittly, showing tensile cracks in the transversal webs.

3.2. Simulation program

For validating the numerical model described in Section 2 we modeled each of the experimental setups described above. While Bitterli and Salmanpour [26,27] investigated the influence of the bed joint incline in increments of 15°, we did simulations in increments of 5° (see Fig. 4). Additionally, we defined upper and lower bounds for the material properties (see Section 3.2.3). Hence, a total of 38 simulations were performed in the FE software Abaqus. Similar to the naming convention of the experiments, we refer to the simulations with a prefix "S" to the incline angle. Additionally, "-max" or "-min" is appended to clarify, if the upper or lower bounds of the material properties were used. We derived the geometry, boundary conditions, and material properties for the numerical models from the experimental study, as shown next.

3.2.1. Geometry and mesh

The geometric definition of the FE model follows the unit-cell concept described in Section 2.1. Hence, a cuboid part, which is two blocks high and one block wide, was extracted from the specimen (see Fig. 7). The FE model consists of six block parts, with an offset of half a block width. These parts are connected with the previously described interface properties in the head joints and the bed joints (see Fig. 7). Notably, in the bed joints the transversal webs are mostly not on top of each other due to the horizontal offset. Thus, the surfaces are only connected, where webs were directly on top of each other, leading to a total contact ratio of 64 % in the bed joints. In contrast, the surfaces in the head joints are fully in contact.

The model consists of 107 326 linear eight-node brick elements (C3D8) and 146 646 nodes. In the framework of the XFEM, cracks were allowed to form anywhere in the model, with one restriction: no crack was allowed to initiate within a radius of 20 mm from an existing crack tip.

3.2.2. Boundary conditions

Although each simulation has a different bed joint incline, the geometry and the mesh remain constant for each simulation. Instead of changing the geometry, the boundary conditions were adapted to obtain the desired macroscopic stress state. Therefore, the loading had to be rotated and split up into its components parallel and perpendicular to the bed joints.

We defined two coordinate systems to distinguish between two levels of observation: the *global coordinates* $1-2-3$, which follow the orthogonal boundaries of the specimen, and the *local coordinates* $x-y-z$, which follow the orthogonal system of mortar joints and are already shown in Figs. 1 and 2 (see Fig. 8). In the global coordinate system, the 3-direction is parallel to the uniaxial loading direction (vertical). The plane spanned by the 1- and 3-axis is parallel to the wall's surface. Hence, the 2-axis is perpendicular to this surface. While the global coordinate system is similar in each specimen, the local coordinate system depends on the bed joint incline. It is obtained by rotating the global coordinate system around the 2-axis by the bed joint incline, leading to the x-axis being parallel to the bed joints, the z-axis being parallel to the head joints, and the y-axis coinciding with the 2-axis.

Considering the experimental setup, in the global coordinate system a uniaxial stress state can be assumed in the middle of the specimen. This stress state was rotated by the angle of incline to obtain the equivalent macroscopic stress state in local coordinates:

$$\bar{\boldsymbol{\sigma}}_{\text{local}} = \boldsymbol{R}(\alpha) \cdot \bar{\boldsymbol{\sigma}}_{\text{global}} \cdot \boldsymbol{R}^{\text{T}}(\alpha)$$
$$= \begin{bmatrix} \cos(\alpha) & -\sin(\alpha) \\ \sin(\alpha) & \cos(\alpha) \end{bmatrix} \cdot \begin{bmatrix} 0 & 0 \\ 0 & \bar{\sigma}_{33} \end{bmatrix} \cdot \begin{bmatrix} \cos(\alpha) & \sin(\alpha) \\ -\sin(\alpha) & \cos(\alpha) \end{bmatrix}, \quad (13)$$

with the rotation matrix $\boldsymbol{R}$.

Knowing the desired local macroscopic stress state, the related local macroscopic strain tensor $\bar{\boldsymbol{\varepsilon}}_{\text{local}}$ was calculated according to Hooke's law as

$$\bar{\boldsymbol{\varepsilon}}_{\text{local}} = \bar{\mathbb{C}}_{\text{local}}^{-1} : \bar{\boldsymbol{\sigma}}_{\text{local}}, \quad (14)$$

with the local macroscopic stiffness tensor $\bar{\mathbb{C}}_{\text{local}}$. This stiffness tensor was found by a numerical stiffness homogenization procedure, utilizing the unit cell approach. The five necessary components of the stiffness tensor could be derived by deliberately eliminating strain components in Hooke's law. Hence, simulating the three strain states LC1–LC3 in Table 1 was sufficient for deriving the local macroscopic stiffness tensor as

$$\bar{\mathbb{C}}_{\text{local}} = \begin{bmatrix} \dfrac{\bar{\sigma}_{xx}^{\text{LC1}}}{\bar{\varepsilon}_{xx}^{\text{LC1}}} & \dfrac{\bar{\sigma}_{xx}^{\text{LC2}}}{\bar{\varepsilon}_{zz}^{\text{LC2}}} & 0 \\[2mm] \dfrac{\bar{\sigma}_{zz}^{\text{LC1}}}{\bar{\varepsilon}_{xx}^{\text{LC1}}} & \dfrac{\bar{\sigma}_{zz}^{\text{LC2}}}{\bar{\varepsilon}_{zz}^{\text{LC2}}} & 0 \\[2mm] 0 & 0 & \dfrac{\bar{\sigma}_{xz}^{\text{LC3}}}{\bar{\varepsilon}_{xz}^{\text{LC3}}} \end{bmatrix}. \quad (15)$$

After calculating the local macroscopic strain components with Eq. (14), the primary node displacements for each simulation could be derived by a linear combination of the three cases in Table 1. Table 2 gives an overview of the calculated components for the seven experiments conducted by Bitterli and Salmanpour [26,27].

3.2.3. Material parameters
Fired clay blocks

For defining the orthotropic stiffness behavior, we used nine independent parameters, given in the material orientation L-T-Z: the Young's moduli E_{LL}, E_{TT}, E_{ZZ}, the Poisson's ratios ν_{TZ}, ν_{LZ}, ν_{LT}, and the shear moduli G_{TZ}, G_{LZ}, G_{LT} (see Table 3). The Young's modulus in Z-direction, E_{ZZ}, could be back-calculated from single-block experiments. With this value as a basis, the other Young's moduli, as well as the shear moduli, were scaled by the ratios obtained from Buchner et al. [1], considering transversally isotropic material behavior. The Poisson's ratios were estimated with the experimentally obtained data from Hannawald [40]. Note, that the parameters refer to the local L-T-Z coordinate system shown in Fig. 1.
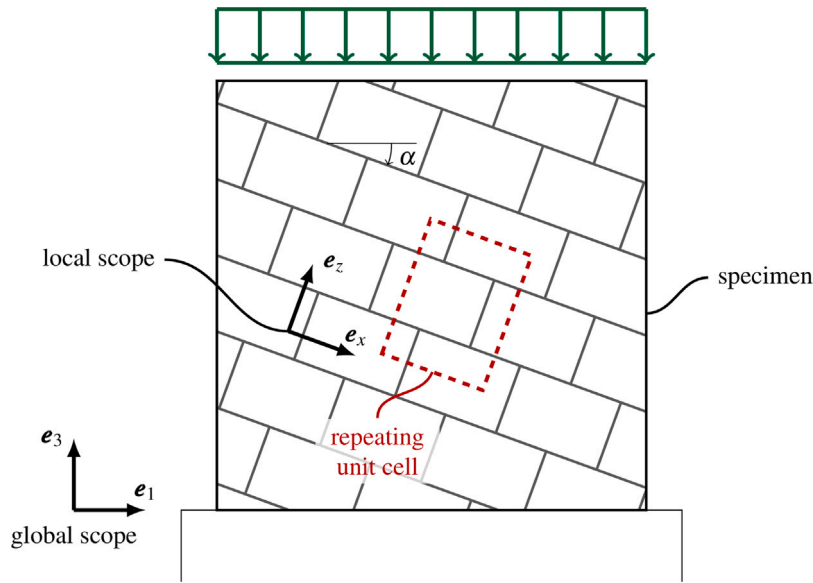
Fig. 8. Definition of the local and global coordinate system. Rotating the global coordinate system around the *y*-axis by the angle of incline α leads to the local coordinate system. The dashed line marks the boundaries of the repeating unit cell, which was used for defining the FE model in Fig. 7.

Table 2
Prescribed stresses and strains for the simulated experiments.

ID	α	$\bar{\sigma}_{xx}$	$\bar{\sigma}_{zz}$	$\bar{\sigma}_{xz}$	$\bar{\varepsilon}_{xx}$	$\bar{\varepsilon}_{zz}$	$\bar{\varepsilon}_{xz}$
S00	0°	0.00 MPa	−10.00 MPa	0.00 MPa	0.14×10^{-3}	-1.69×10^{-3}	0.00
S15	15°	−0.67 MPa	−9.33 MPa	−2.50 MPa	-0.07×10^{-3}	-1.57×10^{-3}	-0.83×10^{-3}
S30	30°	−2.50 MPa	−7.50 MPa	−4.33 MPa	-0.63×10^{-3}	-1.23×10^{-3}	-1.45×10^{-3}
S45	45°	−5.00 MPa	−5.00 MPa	−5.00 MPa	-1.40×10^{-3}	-0.78×10^{-3}	-1.67×10^{-3}
S60	60°	−7.50 MPa	−2.50 MPa	−4.33 MPa	-2.17×10^{-3}	-0.32×10^{-3}	-1.45×10^{-3}
S75	75°	−9.33 MPa	−0.67 MPa	−2.50 MPa	-2.74×10^{-3}	0.02×10^{-3}	-0.83×10^{-3}
S90	90°	−10.00 MPa	0.00 MPa	0.00 MPa	-2.94×10^{-3}	0.14×10^{-3}	0.00

Table 3
Transversally isotropic stiffness parameters for fired clay and the interface stiffness parameters mortar.

Fired clay					Mortar joints	
$E_{LL} = E_{ZZ}$	E_{TT}	$v_{TZ} = v_{LZ} = v_{LT}$	$G_{TZ} = G_{LT}$	G_{TZ}	K_{nn}	$K_{ss} = K_{tt}$
13 500 MPa	8738 MPa	0.2	3500 MPa	5500 MPa	660 N/mm	275 N/mm

The nine strength parameters for defining the Hoffman criterion, the compressive strengths $\sigma_{c,L}$, $\sigma_{c,T}$, $\sigma_{c,Z}$, the tensile strengths $\sigma_{t,L}$, $\sigma_{t,T}$, $\sigma_{t,Z}$, and the shear strengths $\sigma_{s,L}$, $\sigma_{s,T}$, $\sigma_{s,Z}$, were found similar to the stiffness parameters. Salmanpour [27] obtained the compressive strength in Z-direction from compressive tests on single blocks according to EN 772-1 [47]. Using this parameter as a basis, the other compressive strengths, as well as the tensile strengths were scaled according to typical ratios for fired clay provided by Kiefer et al. [23] (see Table 4). Considering the standard deviation of the compressive strength in Z-direction [27], minimum and maximum values were defined. For estimating each shear strength τ_{ij} an upper and lower bound was found from the corresponding tensile strengths, $\sigma_{t,i}$ and $\sigma_{t,j}$, and compressive strengths $\sigma_{c,i}$ and $\sigma_{c,j}$ [19] as

$$\tau_{ij,\min} = \frac{\sigma_{t,i} + \sigma_{t,j}}{2} \text{ and } \tau_{ij,\max} = \frac{\sigma_{c,i} + \sigma_{c,j}}{4}. \tag{16}$$

The mean value of these bound values was used as shear strength for the simulations.

Mortar joints

From experiments on mortar prisms according to EN 1015-11 [48], Salmanpour [27] obtained the compressive strength $f_m = 10.5$ MPa and flexural strength $f_{mq} = 2.8$ MPa. Additionally, he found the Young's modulus of the mortar, $E_m = 6600$ MPa, in non-destructive compression tests. Hence, the stiffness parameters for the cohesive behavior

Table 4
Transversally isotropic strength parameters for fired clay in MPa.

	Tension			Compression			Shear		
	$\sigma_{t,L}$	$\sigma_{t,T}$	$\sigma_{t,Z}$	$\sigma_{c,L}$	$\sigma_{c,T}$	$\sigma_{c,Z}$	$\sigma_{s,TZ}$	$\sigma_{s,LZ}$	$\sigma_{s,LT}$
% of $\sigma_{c,Z}$	29.0	20.0	29.0	100.0	77.0	100.0[a]	34.4[b]	39.5[b]	34.4[b]
Min in (MPa)	7.009	4.834	7.009	24.17	18.61	24.17	8.308	9.547	8.308
Max in (MPa)	8.245	5.686	8.245	28.43	21.89	28.43	9.773	11.23	9.773

[a] Reference value experimentally obtained by [27].
[b] Calculated according to Eq. (16).

approach were calculated as $K_{nn} = 660$ N/mm, and $K_{ss} = K_{tt} = 275$ MPa, using Eq. (9) with a joint thickness $t = 10$ mm and Poisson's ratio $v = 0.2$. Additionally, the pressure-overclosure formulation in Fig. 3 was calibrated with the Young's modulus and compressive strength.

The strength parameters for the cohesive surfaces, the initial shear strength $\tau_{m,ini}$ and the tensile strength $\sigma_{f,\perp}$, and the friction parameter μ_m, were back-calculated from shear tests on masonry triplets (see Fig. 9b) [26,27] with an additional FE model, as discussed next. Considering the symmetry plane in the middle of the triplet, the model consisted of one full clay block, one half clay block, and two steel plates (see Fig. 9a). The lower steel plate was fixed in *x-*, *y-* and *z*-direction along a line parallel to the *y*-axis, allowing rotations around this direction. Additionally, a displacement symmetry condition was
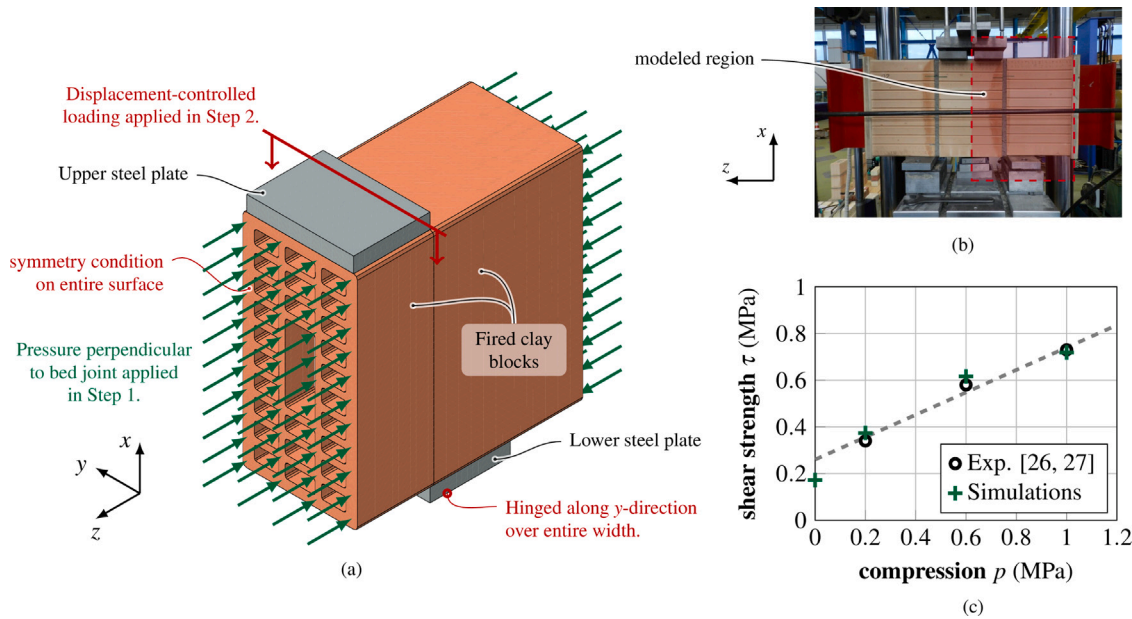
Fig. 9. The strength parameters for the mortar joints were derived by simulating shear tests on masonry triplets [26,27]. (a) Finite element model, (b) experimental setup (from [26,27]), and (c) comparison of numerically and experimentally obtained results.

applied to the surface in the middle block, acting as a symmetry plane. The loads were applied in the following two steps: In the first step, we applied a pressure perpendicular to the bed joint (z-direction). In the second step, we fixed this pressure and applied a displacement in x-direction to the upper steel plate, eventually leading to a peak shear stress of the joint under the given pressure in z-direction.

Following this procedure we created four models with different pressure in z-direction, i. e. 0.0 MPa, 0.2 MPa, 0.6 MPa, as well as 1.0 MPa, and optimized the parameters of the interface damage criterion (Section 2.2.2) to obtain peak shear stresses in good agreement with the experiments performed by Bitterli and Salmanpour [26,27]. Hence, these parameters were chosen with $\mu_{\mathrm{m}} = 0.3$, $\sigma_{\mathrm{f},\perp} = 0.3$ MPa and $\tau_{\mathrm{m,ini}} = 1.4$ MPa, leading to the results in Fig. 9c.

Salmanpour [27] also provided a standard deviation of 13.2 % for the flexural strength. This value was used to define lower and upper bound values for the strength parameters similar to the fired clay blocks (see Table 4) considering a normal distribution.

3.2.4. Computational aspects

For overcoming numerical problems related to the initiation of contact between two surfaces, an additional step was introduced at the beginning of the calculation. In this step, the displacements of each primary node were set to zero. Due to the chosen pressure-overclosure formulation with an insignificant compressive contact stress at zero distance between the surfaces, contact could be ensured in each relevant point, before the displacement-controlled loading was applied in the following step.

The simulations were performed on a high-performance computing cluster with 168 CPUs in total. Using eight CPU cores in parallel, one simulation took approximately 700 minutes on average to finish.

4. Results and discussion

Using the presented numerical approach we were able to identify not only the peak stresses but also the relations between the loading direction and occurring stresses, as well as three key mechanisms leading to failure (see Figs. 10 to 12 and Table 5). We begin by describing these results and comparing them to the experimental observations from Bitterli and Salmanpour [26,27].

A vertical compressive load leads to vertical compressive stresses in the longitudinal webs, compressive stresses perpendicular to the bed joint, and tensile horizontal stresses in the transversal webs. The reason for these horizontal stresses, which are critical for failure, lies in the structural composition of the blocks and was described in [19]: Due to the offset of the blocks, some of the transversal webs are positioned not directly on top of each other. Therefore, the vertical compressive stresses are redistributed to the longitudinal webs, leading to tensile stresses in the transversal webs. Thus, under mainly vertical compressive loading (S00, S15, and S30), tensile cracks in the transversal webs led to failure (mechanism I, see Fig. 10a). Failure in the corresponding experiments (E00, E15, and E30) was governed by vertical cracks beginning in the head joints and spalling of the outermost longitudinal webs (see Fig. 10b). The observed spalling can be traced back to the tensile cracks mentioned above, as Kiefer et al. [23] stated.

Shear loads lead to shear stresses in the joints as well as the longitudinal webs. Due to the inhomogeneous nature of a masonry wall, shear loads additionally lead to a rotation of the blocks within the wall, introducing bending moments in the joints [49]. These bending moments induce stresses perpendicular to the joints, i. e., tension on one side of the block and compression on the other side, leading again to horizontal stresses in the transversal webs, as described above. In combination with large vertical compressive loads, the stresses perpendicular to the bed joint are entirely compressive. In contrast, for smaller vertical compressive loads tensile stresses perpendicular to the bed joints may be crucial for joint failure. Additionally, the shear strength of the mortar increases with compressive stresses perpendicular to the joint. Hence, for shear loads, the failure mechanism strongly depends on the load magnitude in the local z-direction.

With increasing shear and decreasing vertical compressive stresses (S30, S45, S60, and S75), shear failure of the bed joints was the governing failure mechanism, manifesting in a sliding deformation along the bed joint (mechanism II, see Fig. 11a). The same mechanism could be observed in the corresponding experiments (see Fig. 11b). S75 showed a slightly different mechanism from the other simulations: Due to the small amount of vertical compressive stresses, tensile stresses introduced damage to the mortar joints. This damage led to a reduced contact area between the blocks, which again triggered shear failure of the joints. Hence, with larger vertical compressive forces, pure shear failure occurred, while with lower vertical compressive forces a combination of tensile and shear failure was relevant.
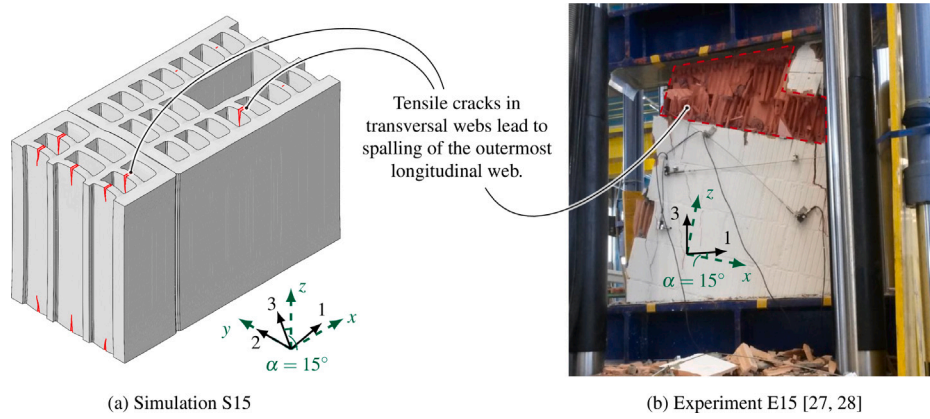
(a) Simulation S15

Tensile cracks in transversal webs lead to spalling of the outermost longitudinal web.

(b) Experiment E15 [27, 28]

Fig. 10. Failure mechanism I – Failure under vertical compressive loading was governed by tensile cracks in the transversal webs and subsequent spalling of the outermost longitudinal webs.
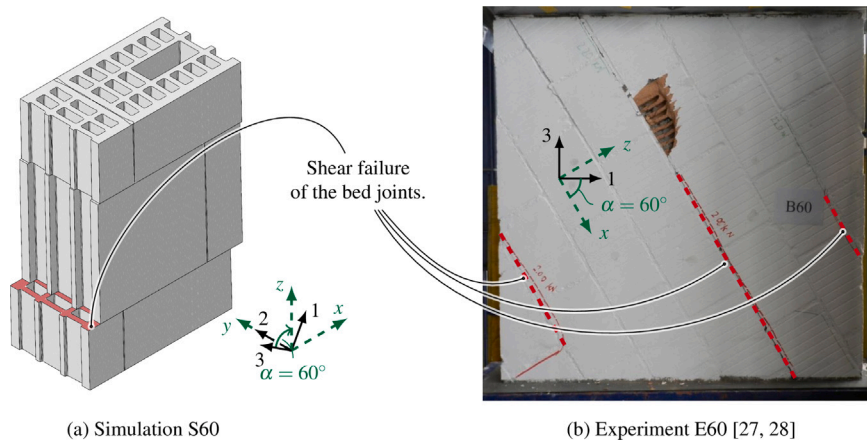

(a) Simulation S60

Shear failure of the bed joints.

(b) Experiment E60 [27, 28]

Fig. 11. Failure mechanism II — Failure under shear loads was governed by shear failure of the mortar joints. The dashed red lines in (b) mark the regions, where shear failure occurred in the experiments.

Horizontal compressive loads are mostly transferred via horizontal compressive stresses in the longitudinal webs and horizontal compressive stresses in the head joints. These compressive stresses lead to deformations in the mortar head joint in local x-direction, which are larger at the outermost longitudinal webs. This deformation difference between the outermost longitudinal webs and their direct neighbors introduces bending moments in the connecting transversal webs, leading to critical tensile stresses in the connection between transversal and longitudinal webs. Thus, under horizontal compressive loading (S90) tensile cracks in the connection between transversal and longitudinal webs led to failure (mechanism III, see Fig. 12a). Again, in the corresponding Experiment (E90) spalling of the outermost longitudinal web was observed in some areas, indicating detachment of these webs. On the left and right sides of the specimen, cracks could be found in similar locations as the simulation predicted (see Fig. 12b).

Next, we are going to compare the numerically obtained peak stresses with the experimental results. Therefore, we rotated the evaluated peak stress state $\bar{\sigma}^{f,\alpha}_{\text{local}}$ from the local scope back to the global scope with Eq. (13) and the negative value of bed joint incline α. While, theoretically, only the stress component $\bar{\sigma}^{f,\alpha}_{33}$ should be non-zero after rotation, the non-linearities in the calculations led to other components also being non-zero. Nevertheless, these components were significantly smaller than the desired macroscopic global stress in the 3-direction. Hence, for each simulation the component $\bar{\sigma}^{f,\alpha}_{33}$ is compared to the corresponding experimentally obtained peak stress ($f_{m\alpha}$ in Fig. 6) in Fig. 13 and Table 5.

While each green circle in Fig. 13 denotes the peak stress of one experiment, the gray area represents the range between the upper and

Table 5
Comparison of numerically and experimentally obtained global macroscopic peak stresses $\bar{\sigma}^{f,\alpha}_{33}$ and observed failure mechanisms.

Simulations				Experiments [26,27]		
	Peak stress (MPa)		Failure		Peak stress	Failure
	Min	Max	mechanism		(MPa)	mechanism
S00	4.35	5.46	I	E00	5.35	I
S15	3.90	4.90	I	E15	4.13	I
S30	2.53	3.03	I, II	E30	2.19	I, II
S45	1.22	1.54	II	E45	1.35	II
S60	1.16	1.45	II	E60	1.22	II
S75	1.87	2.54	II	E75	1.19	II
S90	2.81	3.61	III	E90	2.03	III

I ... Tensile cracks in the transversal webs leading to spalling of outermost longitudinal webs (Fig. 10).
II ... Shear failure of the bed joints (Fig. 11).
III ... Tensile cracks in the transversal webs due to bending of these webs (Fig. 12).

lower boundary of the numerically obtained results. Hence, four out of seven experimentally obtained peak stresses (E00, E15, E45, and E60) are within the upper and lower bounds of the simulation results. E30 delivers a peak stress 13 % below S30-min, which is still acceptably close to the simulation results.

The simulations exhibit the most significant deviations from the experimental results at S75 and S90, with discrepancies of 57 % and 38 %. One possible explanation for this variation is the drying stage that freshly extruded blocks undergo before firing. During this drying process, the intersections between the webs require more time to dry
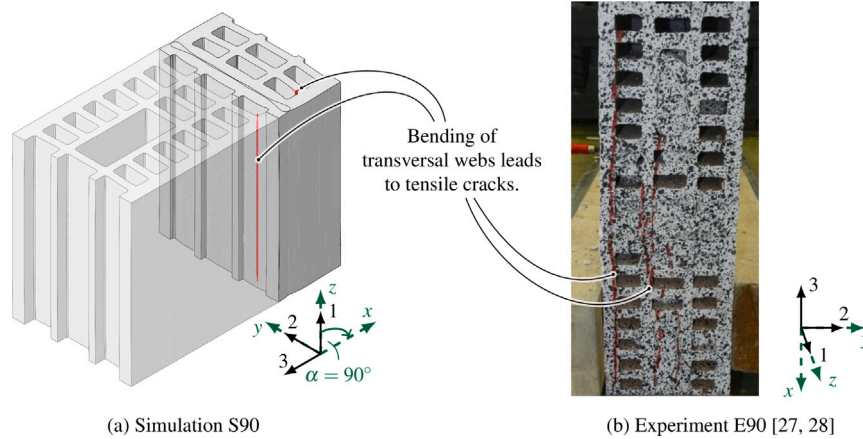
(a) Simulation S90   (b) Experiment E90 [27, 28]

Fig. 12. Failure mechanism III — Failure under horizontal compressive loads was governed by tensile cracks in the connection between transversal and longitudinal webs. The image in (b) shows the side view of the specimen. The red lines mark where cracks occurred.
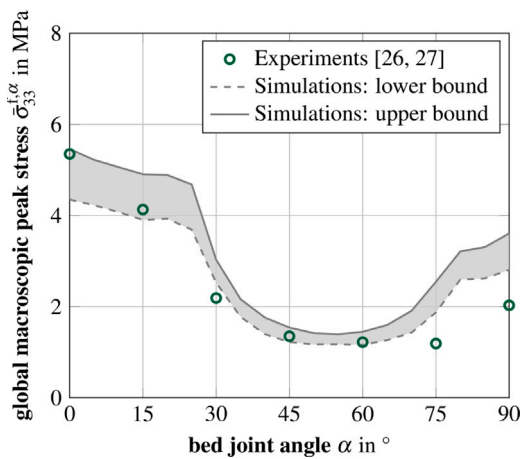

Fig. 13. Comparison of numerically and experimentally obtained peak stresses. We obtained the lower and upper bounds of the simulations by using the minimum and maximum material properties defined in Sections 2.2.1 and 3.2.3.
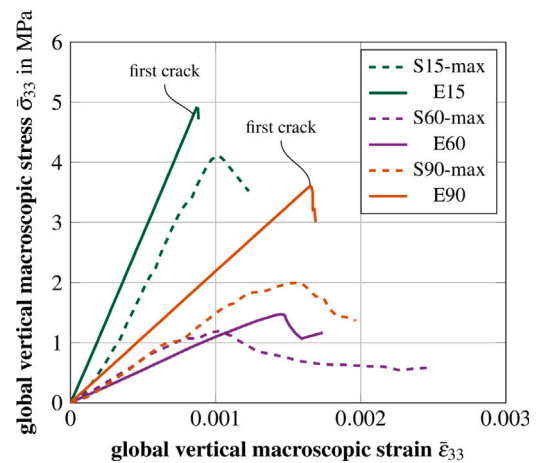

Fig. 14. Numerically obtained stress–strain relations (solid lines) compared to the experimental results (dashed lines) for $\alpha \in [15°, 60°, 90°]$. The upper bound of the simulation results was used (max).

due to the reduced ratio of surface area to clay mass. Consequently, the difference in material shrinkage increases the likelihood of microstructural defects in these intersections [50], which we did not account for in our analysis.

However, this deviation leads to a less distinct material anisotropy in the simulations compared to the experimentally obtained peak stresses. This anisotropy can be captured by the ratio of the horizontal compressive masonry strength to the vertical counterpart, $f_{m,x}/f_{m,z}$, which is 0.661 in the simulations and 0.379 in the experiments. For different types of vertically perforated block masonry, this value ranges approximately from 0.25 up to 0.63, depending on the amount and position of cavities in the block design [6]. Thus, the model underestimates the material anisotropy for this case and would benefit from implementing the discussed strength reduction due to the drying process.

Overall, the numerically obtained peak stresses follow a similar trend as the experimental results. Notably, the lowest peak stress for shear failure occurs at around $\alpha = 60°$, although the largest shear stress component occurs at $\alpha = 45°$ (see also Table 2). The reason for that is the dependency of the shear strength on the compressive stresses perpendicular to the bed joints: While the amount of shear loads is decreasing from S45 to S60, the vertical compressive stresses are also decreasing, leading to a smaller shear strength.

Last but not least, we compare the numerically obtained stress–strain relations ($\bar{\sigma}_{33}$–$\bar{\varepsilon}_{33}$) with the experimental results (see Fig. 14).

Thereby, we focus on the results of the three simulations S15, S60, and S90, each representative of one failure mechanism.

Simulation S15 behaved linearly until the peak stress was reached, followed by an abrupt drop in stresses. The corresponding experiment E15 showed a lower stiffness than the simulation in the beginning, with a gradually increasing gradient afterward. After the gradient increased to a constant value, the experimentally obtained curve is almost parallel to the numerically obtained curve. Hence, the effective vertical stiffness of the unit cell is comparable to the real stiffness properties.

Simulation S60 behaved nearly linear until the peak stress, showing a minor decrease of the gradient starting at 60 % of the peak stress. The stress decrease after the peak stress was reached is less abrupt than at S15. After a 13.5 % decrease the stress increased again linearly, because of the frictional properties of the interface and the still increasing stress perpendicular to the bed joint. Compared to the corresponding experiment E60, the simulation behaved slightly softer before the peak stress was reached and less ductile afterward.

Simulation S90 behaved linearly until the peak stress was reached, followed by an abrupt drop in stresses, similar to simulation S15. The corresponding experiment E90 showed an approximately 23 % lower stiffness than the simulation and significantly more ductile post-peak behavior.

Notably, our simulations showed markedly fewer pre-peak nonlinearities compared to the experimental results. The root of this discrepancy lies in the inherent nature of the unit cell approach. In an
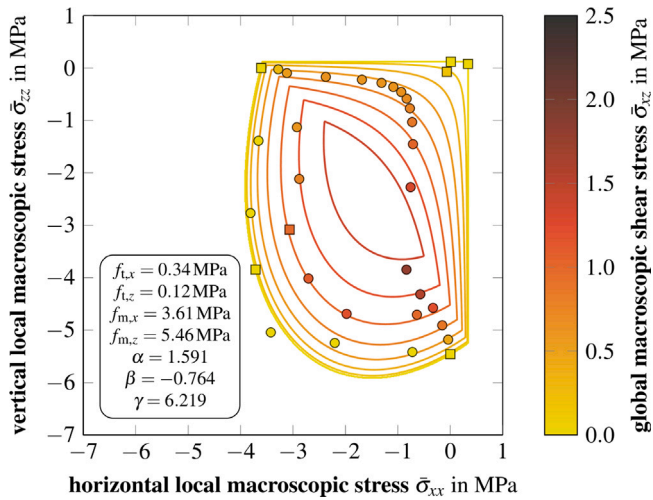
Fig. 15. Local macroscopic peak stress states for 34 simulations with different in-plane loading (circles ● and squares ■) compared to a Rankine–Hill surface gained from simulating seven load combinations (squares ■) proposed by Lourenço [6] (see Appendix B). The upper material limits (max) were used. The stresses are given in local coordinates $x - y - z$.

experimental setting, if damage occurs at one point, the load can be redistributed to the intact portions of the specimen. However, due to the periodic boundary conditions of the unit cell approach, any failure-inducing mechanism is subsequently repeated, which contrasts with the resilience observed in real-world experiments.

Motivated by the good agreement of the failure mechanisms and the peak stresses with the experimental results, we simulated additional loading combinations to obtain enough results for fitting a Rankine–Hill surface. Lourenço [6] proposed seven loading combinations for easily defining the failure surface. Two of these loading combinations, horizontal and vertical uniaxial compression (S90 and S00, respectively), are already included in the simulations presented above. Applying the remaining five loading combinations on the numerical model and evaluating the peak stresses with the same failure criterion as above, led to the parameters for the Rankine–Hill surface displayed in Fig. 15 (see also Appendix B). The coefficient of determination of the surface compared to the simulations is 0.76. Comparing the peak stresses obtained from simulations S00–S90 to the corresponding load combinations on the Rankine–Hill surface, a good agreement can also be seen (Fig. 16(a), green circles). Notably, the first significant decrease of the peak stress occurs earlier and the plateau at a larger joint incline is also reached earlier. Hence, the smallest peak stress occurs around $\alpha = 50°$ instead of $\alpha = 60°$.

While each simulation in the compression regime failed in one of the previously discussed failure mechanisms (i.e., I, II, and III), two simulations in the tensile regime showed another mechanism: tensile failure perpendicular to the joints. Since none of the experiments conducted by Bitterli and Salmanpour [26,27] showed a comparable loading or failure mechanism, we were not able to validate these two results. However, these simulations only have a minor impact on the overall fit of the surface.

The Rankine–Hill surface is capable of qualitatively capturing the failure envelope of masonry in general [6]. Therefore, the good agreement with the simulations underlines the validity of the obtained peak stresses with different loading combinations.

In addition to the fitted Rankine–Hill surface, Fig. 16 contains further failure surfaces (Fig. 16(a)) and experiments (Fig. 16(b)) from literature, compared to the simulation results. Another failure surface beside the Rankine–Hill surface, which is applicable for vertically perforated clay block masonry, is the surface developed by Ganz [5]. He analytically defined each part of the failure envelope as a function

of geometry and material properties. Calibrated with the block geometry and simulation results (see Appendix A), the failure surface after Ganz [5] is also similar to the simulation results (Fig. 16(a), orange crosses). Additionally, we approximated the envelope for shear failure of the bed joint as a function of the incline angle α and the results of the shear tests on masonry triplets ($\tau_{m,ini}$ and μ_m). Therefore, we calculated the macroscopic shear stress from the incline angle α and compared it to the shear strength, obtained from the shear test results using a Mohr–Coulomb criterion, leading to the following relation for calculating the peak stress:

$$\bar{\sigma}_{33}^{f,\alpha} = \frac{2 \cdot \tau_{m,ini} \cdot \sin(\alpha) \cdot \cos(\alpha)}{1 - \sin^4(\alpha) + 2 \cdot \mu_m \cdot \cos^3(\alpha) \cdot \sin(\alpha) + \cos^4(\alpha)}. \tag{17}$$

Notably, each of the curves in Fig. 16(a) has the same overall shape, where the first part before the sudden drop is governed by block failure, the second part from the drop to reaching the plateau is governed by shear failure, and the third part is again governed by block failure.

The simulation results are compared with three sets of experimental data in Fig. 16(b). To facilitate a better comparison, the values of each series were normalized by their global peak stress at $\alpha = 0°$. Dialer [51] and Page [52] performed uniaxial and biaxial tests on solid clay block masonry with different angles of bed joint incline. Additionally, we found a similar relation for experiments on layered rock [53]. Although the curves are quite different, they all share the same overall trend: a decreasing peak stress with increasing bed joint incline, with a minimum between 45° and 75°, followed by an increasing peak stress.

5. Conclusion and outlook

This work describes the development of a numerical model for computing the peak stress of vertically perforated clay block masonry under arbitrary in-plane loads. The previously published model [19,23] was extended by introducing a realistic material model for the mortar joints. These modeling strategies were combined to simulate a series of experiments with different combinations of biaxial compressive loading and shear loading [27]. The obtained peak stresses were mostly in good agreement with the experimental results. Solely under horizontal compression, the model yielded larger peak stresses, resulting in a less distinct anisotropy, compared to the experiments. Additionally, the three main failure mechanisms observed in the experiments could be realistically replicated with the numerical model. While the failure mechanisms under vertical compression and shear were already published in the literature (e. g. [19,23,42,52]), for the first time the failure under horizontal compressive loading could be linked to deformation differences in the head joint.

After the validation, a Rankine–Hill surface for the given clay block masonry could be fitted by simulating the seven load combinations proposed by Lourenço [6]. This surface nicely matched the numerically obtained peak stresses with the loading combinations investigated by Bitterli and Salmanpour [26,27]. Additionally, the failure surface proposed by Ganz [5], a criterion for shear failure derived from the mortar parameters, and various experimental series showed qualitatively similar behavior to the numerical results, showcasing their validity.

Thus, the model can be used to generate failure surfaces for different masonry products to be used as a macroscopic failure criterion within FE software. Another application is a parameter study on different geometrical features or material properties, to find the most significant parameters for increasing the macroscopic strength under given boundary conditions. This helps to gain a deeper understanding of the behavior of clay block masonry under in-plane loading.

Although the presented FE model provided valuable insights, the model would benefit from further improvements to better capture the anisotropic behavior. One potential enhancement lies in incorporating reduced strengths in the connection between longitudinal and transversal webs. This adjustment is particularly relevant as mechanical
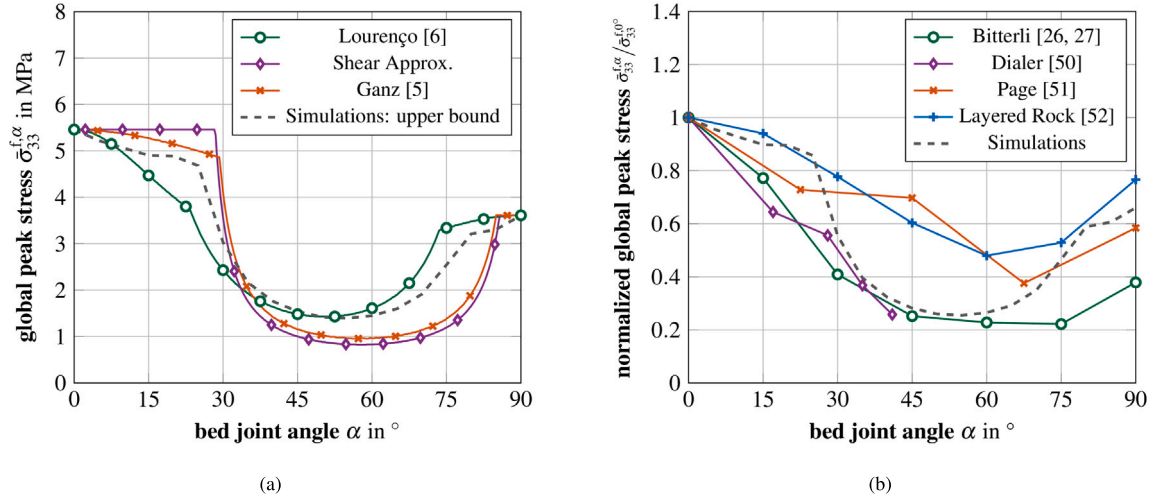
Fig. 16. Comparison of the numerically obtained peak stresses with other findings: (a) failure surfaces for the upper bound of material properties, (b) normalized experimental data [26,27,51–53].

defects are prone to occur in these regions during the drying process. Future research should focus on refining the FE model to effectively account for these localized effects and improve the overall predictive capabilities in this context.

For future studies, another interesting modification of the model would be the adoption of the phase field method (refer e. g. to Miehe et al. [54]) as an alternative to XFEM. In contrast to XFEM, the phase field method offers notable advantages by utilizing a diffusive representation of cracks instead of introducing sharp discontinuities. This approach is known to be very stable, even for complex crack topologies, as e. g. Pech et al. showed for complex wood structures with anisotropic material behavior [55,56].

Overall, the presented model exhibits great potential for optimizing existing products or developing new block designs, making it a valuable tool for enhancing structural performance in the field of clay block masonry.

CRediT authorship contribution statement

Raphael Reismüller: Conceptualization, Methodology, Software, Validation, Formal analysis, Investigation, Writing – original draft, Visualization. **Markus Lukacevic:** Conceptualization, Writing – review & editing. **Sebastian Pech:** Writing – review & editing. **Andreas Jäger:** Conceptualization, Supervision, Project administration, Funding acquisition. **Josef Füssl:** Writing – review & editing, Supervision, Project administration, Funding acquisition.

Declaration of competing interest

The authors declare that they have no known competing financial interests or personal relationships that could have appeared to influence the work reported in this paper.

Data availability

Data will be made available on request.

Acknowledgments

Appendix A. Calibration of the failure surface after Ganz

Ganz [5] proposed a failure surface for masonry with tensile strength, consisting of the following 12 failure criteria:

$$\Phi_{1a} = \bar{\sigma}_{xz}^2 - (\omega_m \cdot f_{m,x} - \bar{\sigma}_{xx})(2\omega_m \cdot f_{m,z} - \bar{\sigma}_{zz}) \le 0. \tag{A.1}$$

$$\Phi_{1b} = (1 + \omega_m)^2 \cdot \bar{\sigma}_{xz}^2 + [\omega_m \cdot (\bar{\sigma}_{zz} + f_{m,z}) - \bar{\sigma}_{xx}] \\ \times [\bar{\sigma}_{zz} + f_{m,z} - f_{m,x} - \omega_m \cdot (\bar{\sigma}_{xx} + f_{m,x})] \le 0. \tag{A.2}$$

$$\Phi_{1c} = (1 + \omega_m)^2 \cdot \bar{\sigma}_{xz}^2 + [\omega_m \cdot (\bar{\sigma}_{zz} - 2\omega_m \cdot f_{m,z} + f_{m,x} \cdot (1 + \omega_m)) - \bar{\sigma}_{xx}] \\ \times [\bar{\sigma}_{zz} - 2\omega_m \cdot f_{m,z} - \omega_m \cdot f_{m,x}] \le 0. \tag{A.3}$$

$$\Phi_2 = \bar{\sigma}_{xz}^2 - (\bar{\sigma}_{xx} + f_{m,x}) \cdot (\bar{\sigma}_{zz} + f_{m,z}) \le 0. \tag{A.4}$$

$$\Phi_{3ab} = \bar{\sigma}_{xz}^2 + \bar{\sigma}_{xx} \cdot (\bar{\sigma}_{xx} + f_{m,x}) \le 0. \tag{A.5}$$

$$\Phi_{3c} = \bar{\sigma}_{xz}^2 + \bar{\sigma}_{xx} \cdot (\bar{\sigma}_{xx} - \omega_m \cdot f_{m,x}) \le 0. \tag{A.6}$$

$$\Phi_{3d} = 4\omega_m \cdot \bar{\sigma}_{xz}^2 - [\omega_m \cdot f_{m,x} - \bar{\sigma}_{xx} \cdot (1 - \omega_m)]^2 \le 0. \tag{A.7}$$

$$\Phi_{4a} = \bar{\sigma}_{xz}^2 - (c - \bar{\sigma}_{zz} \cdot \tan(\varphi))^2 \le 0. \tag{A.8}$$

$$\Phi_{4b} = \bar{\sigma}_{xz}^2 + (\bar{\sigma}_{zz} - f_{t,z} + R_b)^2 - R_b^2 \le 0. \tag{A.9}$$

$$\Phi_{4c} = \bar{\sigma}_{xz}^2 + \left[\bar{\sigma}_{zz} - f'_{t,z} \cdot \left(\frac{\bar{\sigma}_{xx}}{\mu \cdot f_{m,x}} + 1\right) + R_c\right]^2 - R_c^2 \le 0. \tag{A.10}$$

$$\Phi_{4d} = \bar{\sigma}_{xz}^2 \cdot \left(1 + \frac{2 \cdot a_L}{a_S} \cdot \tan(\varphi)\right)^2 - \left(\bar{\sigma}_{zz} \cdot \tan(\varphi) + \bar{\sigma}_{xx} \cdot \frac{2 \cdot a_L}{a_S} - c\right)^2 \le 0. \tag{A.11}$$

$$\Phi_{4e} = \left(|\bar{\sigma}_{xz}| + \frac{2a_L}{a_S} \cdot \bar{\sigma}_{xx}\right)^2 + \left(\bar{\sigma}_{zz} + |\bar{\sigma}_{xz}| \cdot \frac{2a_L}{a_S} - f_{t,z} + R_b\right)^2 - R_b^2 \le 0. \tag{A.12}$$

$$R_b = c \cdot \tan\left(\frac{\pi}{4} + \frac{\varphi}{2}\right) - f_{t,z} \cdot \frac{\sin(\varphi)}{1 - \sin(\varphi)} \tag{A.13}$$

$$R_c = c \cdot \tan\left(\frac{\pi}{4} + \frac{\varphi}{2}\right) - f'_{t,z} \cdot \left(\frac{\bar{\sigma}_{xx}}{\mu \cdot f_{m,x}} + 1\right) \cdot \frac{\sin(\varphi)}{1 - \sin(\varphi)} \tag{A.14}$$

Thereby, $\bar{\sigma}_{xx}$, $\bar{\sigma}_{zz}$, and $\bar{\sigma}_{xz}$ are the in-plane components of the local macroscopic stress tensor. Note, that the indices are different than in the original publication. While Ganz [5] refers to the vertical direction with x and the horizontal direction with y, we use x for the horizontal direction and z for the vertical direction, which is consistent with the local coordinate system used within this work.

For calibration of the surface, 10 parameters are needed, i.e. the uniaxial compressive masonry strengths, $f_{m,x}$ and $f_{m,z}$, the ratio of the tensile strengths to their compressive counterparts, ω_m, the vertical uniaxial tensile masonry strength $f_{t,z}$, the distance of the bed joints, a_L, the distance of the head joints, a_S, the cohesion shear stress and the frictional angle of the joints, c and φ, the tensile strength of the joints, $f'_{t,x}$, and an additional parameter μ. For a detailed description of these properties, we refer to the original publication [5]. We derived the strength parameters from the simulation results as $f_{m,x} = 3.61$ MPa, $f_{m,z} = 5.54$ MPa, $f_{t,z} = 0.12$ MPa, $f'_{t,z} = 0.12$ MPa, and $\omega_m = 0.94$. Furthermore, we gained $a_L = 200$ mm and $a_S = 300$ mm from the block geometry, $c = 0.26$ MPa and $\varphi = 0.48$ from the simulation of the shear tests, and set the additional parameter to $\mu = 1$.

Appendix B. Calibration of the Rankine–Hill surface

The Rankine–Hill surface consists of two failure criteria: a Rankine-type criterion and a Hill-type criterion. The Rankine-type surface is defined in the following manner:

$$f_1 = \frac{(\bar{\sigma}_{xx} - f_{t,x}) + (\bar{\sigma}_{zz} - f_{t,z})}{2} + \sqrt{\left(\frac{(\bar{\sigma}_{xx} - f_{t,x}) - (\bar{\sigma}_{zz} - f_{t,z})}{2}\right)^2 + \alpha \bar{\sigma}_{xz}^2}$$
$$= 0, \tag{B.1}$$

with the parameter α, which defines the size of the attainable shear strength for the Rankine-type surface, the uniaxial tensile strengths $f_{t,x}$ and $f_{t,z}$, and the in-plane components of the local macroscopic stress tensor, $\bar{\sigma}_{xx}$, $\bar{\sigma}_{zz}$, and $\bar{\sigma}_{xz}$.

The Hill-type surface forms a rotated centered ellipsoid, which reads as

$$f_2 = A \cdot \bar{\sigma}_{xx}^2 + B \cdot \bar{\sigma}_{xx} \cdot \bar{\sigma}_{zz} + C \cdot \bar{\sigma}_{zz}^2 + D \cdot \bar{\sigma}_{xz}^2 - 1 = 0. \tag{B.2}$$

The four parameters A, B, C, and D can be derived from the material's tensile strengths, $f_{t,x}$ and $f_{t,z}$, and compressive strengths, $f_{m,x}$ and $f_{m,z}$, in the following way:

$$A = \frac{1}{(f_{m,x})^2}, \quad B = \frac{\beta}{f_{m,x} \cdot f_{m,z}}, \quad C = \frac{1}{(f_{m,z})^2}, \quad \text{and} \quad D = \frac{\gamma}{f_{m,x} \cdot f_{m,z}}, \tag{B.3}$$

with the parameter β, which defines the interaction of axial stresses $\bar{\sigma}_{xx}$ and $\bar{\sigma}_{zz}$ in the compressive regime, and the parameter γ, which defines the size of the attainable shear strength for the Hill-type surface.

Thus, seven parameters are needed to fully calibrate the Rankine–Hill surface, i.e. the uniaxial strengths $f_{t,x}$, $f_{t,z}$, $f_{m,x}$, and $f_{m,z}$, as well

as the parameters α, β, and γ. While we obtained the uniaxial strengths from applying the corresponding uniaxial loading to the FE model, we derived the remaining parameters from simulating three additional loading combinations proposed by Lourenço [6] (see Fig. B.17) using the following equations:

$$\alpha = \frac{1}{9} \cdot \left(1 + 4\frac{f_{t,x}}{f_\alpha}\right) \cdot \left(1 + 4\frac{f_{t,z}}{f_\alpha}\right), \tag{B.4}$$

$$\beta = \left[\frac{1}{f_\beta^2} - \frac{1}{f_{m,x}^2} - \frac{1}{f_{m,z}^2}\right] \cdot f_{m,x} f_{m,z}, \text{ and} \tag{B.5}$$

$$\gamma = \left[\frac{16}{f_\gamma} - 9 \cdot \left(\frac{1}{f_{m,x}^2} + \frac{\beta}{f_{m,x} \cdot f_{m,z}} + \frac{1}{f_{m,z}^2}\right)\right]. \tag{B.6}$$

Hence, we obtained the following parameters for the Rankine–Hill surface: $f_{t,x} = 0.34$ MPa, $f_{t,z} = 0.12$ MPa, $f_{m,x} = 3.61$ MPa, $f_{m,z} = 5.46$ MPa, $\alpha = 1.591$, $\beta = -0.764$, and $\gamma = 6.219$.

Appendix C. Orthotropic Hoffman criterion

The Hoffman criterion uses all six independent components of the stress tensor and is defined as follows:

$$f(\boldsymbol{\sigma}) = C_1 \cdot (\sigma_{TT} - \sigma_{ZZ})^2 + C_2 \cdot (\sigma_{ZZ} - \sigma_{LL})^2 + C_3 \cdot (\sigma_{LL} - \sigma_{TT})^2$$
$$+ C_4 \cdot \sigma_{LL} + C_5 \cdot \sigma_{TT} + C_6 \cdot \sigma_{ZZ} \tag{C.1}$$
$$+ C_7 \cdot (\sigma_{LT})^2 + C_8 \cdot (\sigma_{TZ})^2 + C_9 \cdot (\sigma_{LZ})^2,$$

Hereby, σ_{ij} are the components of the stress tensor given in the material orientation L-T-Z (shown in Fig. 1), and C_1 to C_9 are constants, which are derived from the material's tensile, compressive, and shear strengths, $\sigma_{t,i}$, $\sigma_{c,i}$, and $\sigma_{s,ij}$, respectively:

$$C_1 = \frac{1}{2}\left[\left(\sigma_{t,T} \cdot \sigma_{c,T}\right)^{-1} + \left(\sigma_{t,Z} \cdot \sigma_{c,Z}\right)^{-1} - \left(\sigma_{t,L} \cdot \sigma_{c,L}\right)^{-1}\right], \tag{C.2}$$

C_2 and C_3 by permutation of indices L, T, Z,

$$C_4 = \left(\sigma_{t,L}\right)^{-1} - \left(\sigma_{c,L}\right)^{-1}, \tag{C.3}$$

C_5 and C_6 by permutation of indices L, T, Z,

$$C_7 = \left(\sigma_{s,TZ}\right)^{-2}, \tag{C.4}$$

C_8 and C_9 by permutation of indices L, T, Z..

The Hoffman criterion was implemented using a user subroutine, which can be found in the supplementary material.

Appendix D. Supplementary data

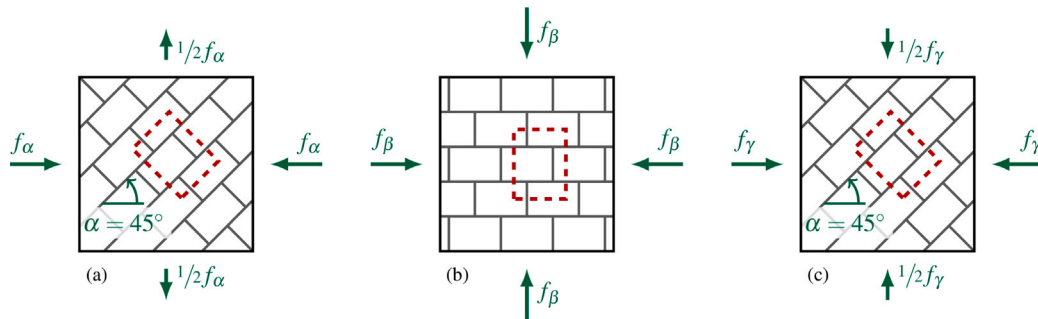Supplementary material related to this article can be found online at https://doi.org/10.1016/j.engstruct.2023.116557.

Fig. B.17. Additional loading combinations proposed by Lourenço [6]. The dashed line marks the boundaries of the repeating unit cell, which was used for defining the FE model in Fig. 7.

References

[1] Buchner T, Kiefer T, Königsberger M, Jäger A, Füssl J. Continuum microme-chanics model for fired clay bricks: upscaling of experimentally identified microstructural features to macroscopic elastic stiffness and thermal conductivity. Mater Des 2021;212:110212. http://dx.doi.org/10.1016/j.matdes.2021.110212.

[2] Buchner T, Kiefer T, Gaggl W, Zelaya-Lainez L, Füssl J. Automated morphomet-rical characterization of material phases of fired clay bricks based on scanning electron microscopy, energy dispersive X-ray spectroscopy and powder X-ray diffraction. Constr Build Mater 2021;288:122909. http://dx.doi.org/10.1016/j.conbuildmat.2021.122909.

[3] Buchner T, Kiefer T, Zelaya-Lainez L, Gaggl W, Konegger T, Füssl J. A multi-technique, quantitative characterization of the pore space of fired bricks made of five clayey raw materials used in European brick industry. Appl Clay Sci 2021;200:105884. http://dx.doi.org/10.1016/j.clay.2020.105884.

[4] Buchner T, Königsberger M, Jäger A, Füssl J. A validated multiscale model linking microstructural features of fired clay brick to its macroscopic multiaxial strength. Mech Mater 2022;170:104334. http://dx.doi.org/10.1016/j.mechmat.2022.104334.

[5] Ganz HR. Mauerwerksscheiben unter Normalkraft und Schub (Ph.D. thesis), ETH Zurich; 1985, p. 133 S.. http://dx.doi.org/10.3929/ETHZ-A-000360363.

[6] Lourenço PB. Computational strategies for masonry structures (Ph.D. thesis), Delft University of Technology; 1996.

[7] Netzel H, Van Zijl GPAG. Nonlinear numerical simulation of settlement-induced damage to solid masonry walls. In: 13th international brick masonry conference, Amsterdam. Citeseer; 2004.

[8] Grande E, Milani G, Sacco E. Modelling and analysis of FRP-strengthened masonry panels. Eng Struct 2008;30(7):1842–60. http://dx.doi.org/10.1016/j.engstruct.2007.12.007.

[9] Da Porto F, Guidi G, Garbin E, Modena C. In-plane behavior of clay masonry walls: experimental testing and finite-element modeling. J Struct Eng 2010;136(11):1379–92. http://dx.doi.org/10.1061/(ASCE)ST.1943-541X.0000236.

[10] Grande E, Imbimbo M, Sacco E. Finite element analysis of masonry panels strengthened with FRPs. Composites B 2013;45(1):1296–309. http://dx.doi.org/10.1016/j.compositesb.2012.09.002.

[11] Rots JG, Messali F, Esposito R, Jafari S, Mariani V. Thematic keynote com-putational modelling of masonry with a view to groningen induced seismicity. In: Structural analysis of historical constructions: anamnesis, diagnosis, therapy, controls. CRC Press; 2016, p. 227–38.

[12] Mininno G, Ghiassi B, Oliveira DV. Modelling of the in-plane and out-of-plane performance of TRM-strengthened masonry walls. Key Eng Mater 2017;747:60–8. http://dx.doi.org/10.4028/www.scientific.net/KEM.747.60.

[13] Bujotzek L, Müller D, Graubner C-A. Monte Carlo simulation of masonry walls in compression considering spatially variable material properties. In: Brick and block masonry-from historical to sustainable masonry. CRC Press; 2020, p. 178–86.

[14] Noor-E-Khuda S. An explicit finite-element modeling method for masonry walls using continuum shell element. J Archit Eng 2021;27(4):04021040. http://dx.doi.org/10.1061/(ASCE)AE.1943-5568.0000518.

[15] Leonetti L, Greco F, Trovalusci P, Luciano R, Masiani R. A multiscale damage analysis of periodic composites using a couple-stress/Cauchy multidomain model: application to masonry structures. Composites B 2018;141:50–9. http://dx.doi.org/10.1016/j.compositesb.2017.12.025.

[16] Bošnjak J, Gambarelli S, Sharma A, Mešković A. Experimental and numerical studies on masonry after exposure to elevated temperatures. Constr Build Mater 2020;230:116926. http://dx.doi.org/10.1016/j.conbuildmat.2019.116926.

[17] Scacco J, Ghiassi B, Milani G, Lourenço PB. A fast modeling approach for numerical analysis of unreinforced and FRCM reinforced masonry walls un-der out-of-plane loading. Composites B 2020;180:107553. http://dx.doi.org/10.1016/j.compositesb.2019.107553.

[18] Segura J, Pelà L, Saloustros S, Roca P. Experimental and numerical insights on the diagonal compression test for the shear characterisation of masonry. Constr Build Mater 2021;287:122964. http://dx.doi.org/10.1016/j.conbuildmat.2021.122964.

[19] Suda R, Kiefer T, Schranz C, Füssl J. A finite-element-based approach to quantify the impact of bed joint reinforcement on the compressive strength of vertically perforated clay block masonry. Eng Struct 2021;239:112277. http://dx.doi.org/10.1016/j.engstruct.2021.112277.

[20] Gaetano D, Greco F, Leonetti L, Lonetti P, Pascuzzo A, Ronchei C. An interface-based detailed micro-model for the failure simulation of masonry structures. Eng Fail Anal 2022;142:106753. http://dx.doi.org/10.1016/j.engfailanal.2022.106753.

[21] Scacco J, Grillanda N, Milani G, Lourenço PB. Novel non-linear static numerical model for curved masonry structures based on a combined adaptive limit analysis and discrete FE computations. Int J Solids Struct 2022;236–237:111265. http://dx.doi.org/10.1016/j.ijsolstr.2021.111265.

[22] Zhou Y, Sluys LJ, Esposito R. An improved mean-field homogenization model for the three-dimensional elastic properties of masonry. Eur J Mech A Solids 2022;96:104721. http://dx.doi.org/10.1016/j.euromechsol.2022.104721.

[23] Kiefer T, Kariem H, Lukacevic M, Füssl J. The compressive strength of vertically perforated clay block masonry predicted by means of a unit-cell type numer-ical simulation tool taking discrete cracking into account. Constr Build Mater 2017;150:24–34. http://dx.doi.org/10.1016/j.conbuildmat.2017.05.201.

[24] Belytschko T, Black T. Elastic crack growth in finite elements with minimal remeshing. Internat J Numer Methods Engrg 1999;45(5):601–20. http://dx.doi.org/10.1002/(SICI)1097-0207(19990620)45:5<601::AID-NME598>3.0.CO;2-S.

[25] Hoffman O. The brittle strength of orthotropic materials. J Compos Mater 1967;1(2):200–6. http://dx.doi.org/10.1177/002199836700100210.

[26] Bitterli S. Versuche an Mauerwerkselementen mit geneigten Lagerfugen (Master's thesis), Zürich: ETH Zürich; 2014.

[27] Salmanpour AH. Displacement capacity of structural masonry (Ph.D. thesis), ETH Zurich; 2017, p. 148. http://dx.doi.org/10.3929/ETHZ-B-000172566.

[28] Reismüller R, Königsberger M, Jäger A, Füssl J. The performance of verti-cally perforated clay block masonry in fire tests predicted by a finite-element model including an energy-based criterion to identify spalling. Fire Saf J 2023;135:103729. http://dx.doi.org/10.1016/j.firesaf.2022.103729.

[29] Böhm HJ. A short introduction to basic aspects of continuum micromechanics. ILSB Report, 2023.

[30] Michel J, Moulinec H, Suquet P. Effective properties of composite materials with periodic microstructure: A computational approach. Comput Methods Appl Mech Engrg 1999;172(1–4):109–43. http://dx.doi.org/10.1016/S0045-7825(98)00227-8.

[31] Lourenço P, Vasconcelos G, Medeiros P, Gouveia J. Vertically perforated clay brick masonry for loadbearing and non-loadbearing masonry walls. Constr Build Mater 2010;24(11):2317–30. http://dx.doi.org/10.1016/j.conbuildmat.2010.04.010.

[32] Celano T, Argiento LU, Ceroni F, Casapulla C. Literature review of the in-plane behavior of masonry walls: theoretical vs. experimental results. Materials 2021;14(11):3063. http://dx.doi.org/10.3390/ma14113063.

[33] Rybicki E, Kanninen M. A finite element calculation of stress intensity factors by a modified crack closure integral. Eng Fract Mech 1977;9(4):931–8. http://dx.doi.org/10.1016/0013-7944(77)90013-3.

[34] Rybicki E, Schmueser D, Fox J. An energy release rate approach for sta-ble crack growth in the free-edge delamination problem. J Compos Mater 1977;11(4):470–87. http://dx.doi.org/10.1177/002199837701100409.

[35] Systèmes D. Abaqus online documentation. 2022.

[36] Bourret J, Tessier-Doyen N, Guinebretiere R, Joussein E, Smith D. Anisotropy of thermal conductivity and elastic properties of extruded clay-based materials: evolution with thermal treatment. Appl Clay Sci 2015;116–117:150–7. http://dx.doi.org/10.1016/j.clay.2015.08.006.

[37] Fódi A. Effects influencing the compressive strength of a solid, fired clay brick. Period Polytech Civ Eng 2011;55(2):117. http://dx.doi.org/10.3311/pp.ci.2011-2.04.

[38] Krueger R. Virtual crack closure technique: history, approach, and applications. Appl Mech Rev 2004;57(2):109–43. http://dx.doi.org/10.1115/1.1595677.

[39] Bocca P, Carpinteri A, Valente S. Fracture mechanics of brick masonry: Size effects and snap-back analysis. Mater Struct 1989;22(5):364–73. http://dx.doi.org/10.1007/BF02472507.

[40] Hannawald J. Determining the tensile softening diagram of concrete-like ma-terials using hybrid optimisation. In: Konsta-Gdoutos MS, editor. Measuring, monitoring and modeling concrete properties. Dordrecht: Springer Netherlands; 2006, p. 179–87. http://dx.doi.org/10.1007/978-1-4020-5104-3_22.

[41] Eis A, Vassilev T. Übersicht über abgeschlossene und laufende forschungsvorhaben im mauerwerksbau. In: Jäger W, editor. Mauerwerk-Kalender 2012. Weinheim, Germany: Wiley-VCH Verlag GmbH & Co. KGaA; 2013, p. 609–47. http://dx.doi.org/10.1002/9783433601617.ch17.

[42] Van der Pluijm R. Out-of-plane bending of masonry : behaviour and strength (Ph.D. thesis), Technische Universiteit Eindhoven; 1999.

[43] Bolhassani M, Hamid AA, Lau AC, Moon F. Simplified micro modeling of partially grouted masonry assemblages. Constr Build Mater 2015;83:159–73. http://dx.doi.org/10.1016/j.conbuildmat.2015.03.021.

[44] Thamboo J, Dhanasekar M. Nonlinear finite element modelling of high bond thin-layer mortared concrete masonry. Int J Mason Res Innov 2016;1(1):5. http://dx.doi.org/10.1504/IJMRI.2016.074727.

[45] Zürcher Ziegeleien AG. SwissModul 15. 2023, https://www.zz-ag.ch/produkte/wand/mauerwerk/swissmodul-15.html.

[46] EN 1052-3. Methods of test for masonry - part 3: determination of ini-tial shear strength. Standard, Brussels, BEL: CEN – European Committee for Standardization; 2002.

[47] EN 772-1. Methods of test for masonry units - part 1: determination of compressive strength. Standard, Brussels, BEL: CEN – European Committee for Standardization; 2016.

[48] EN 1015-11. Methods of test for mortar for masonry - part 11: determination of flexural and compressive strength of hardened mortar. Standard, Brussels, BEL: CEN – European Committee for Standardization; 2019.

[49] Mojsilović N. Zum Tragverhalten von kombiniert beanspruchtem Mauerwerk (Ph.D. thesis), ETH Zurich; 1995, p. 130 S.. http://dx.doi.org/10.3929/ETHZ-A-001549685.

[50] Barbosa de Lima AG, da Silva JB, Almeida GS, Nascimento JJS, Tavares FVS, Silva VS. Clay products convective drying: foundations, modeling and applications. In: Delgado J, Barbosa de Lima AG, editors. Drying and energy technologies, Vol. 63. Cham: Springer International Publishing; 2016, p. 43–70. http://dx.doi.org/10.1007/978-3-319-19767-8_3.

[51] Dialer C. Bruch- und Verformungsverhalten von schubbeanspruchten Mauerwerksscheiben, zweiachsige Versuche an verkleinertem Modellmauerwerk (Ph.D. thesis), München: TU München; 1990.

[52] Page AW. The biaxial compressive strength of brick masonry. Proc Inst Civ Eng 1981;(71):893–906.

[53] Conrad KH. Beeinflussung von technischen Eigenschaften zementgebundener Mörtel durch geeignete Epoxidharzsysteme unter Berücksichtigung der mehrachsialen Festigkeiten (Ph.D. thesis), Grenoble: Institut National Polytechnique de Grenoble; 1986.

[54] Miehe C, Hofacker M, Welschinger F. A phase field model for rate-independent crack propagation: robust algorithmic implementation based on operator splits. Comput Methods Appl Mech Engrg 2010;199(45):2765–78. http://dx.doi.org/10.1016/j.cma.2010.04.011.

[55] Pech S, Lukacevic M, Füssl J. A hybrid multi-phase field model to describe cohesive failure in orthotropic materials, assessed by modeling failure mechanisms in wood. Eng Fract Mech 2022;271:108591. http://dx.doi.org/10.1016/j.engfracmech.2022.108591.

[56] Pech S, Lukacevic M, Füssl J. Validation of a hybrid multi-phase field model for fracture of wood. Eng Fract Mech 2022;275:108819. http://dx.doi.org/10.1016/j.engfracmech.2022.108819.